Low Temperature Physics/Fizika Nizkikh Temperatur, 2016, v. 42, No. 10, pp. 1075–1102

Science and technology of cuprate-based high temperature superconductor thin films, heterostructures and superlattices — the first 30 years

(Review Article)

H.-U. Habermeier

Science Consulting International, Niersteinerstr, 28, Stuttgart D 70499, Germany

Max-Planck-Institute for Solid State Research, Heisenbergstr, 1, Stuttgart D 70569, Germany
E-mail: huh@fkf.mpg.de

Received May 30, 2016, published online August 25, 2016

During the three decades after the discovery of superconductivity at high temperatures in copper oxides, intense research activities generated a tremendous progress in both, mastering the scientific challenges underpinning the understanding of the properties of these chemically and structurally complex materials as well as achieving a mature technology in preparing single phase bulk specimens — including single crystals — and epitaxially grown single crystalline thin films. This review covers in addition to more basic physics oriented developments mainly technological aspects of complex oxide thin film deposition as an enabling technology to explore the physics of these materials. It consists of two parts: after a brief introduction to the materials development prior to the discovery of superconducting copper oxides, a description of the relevant properties of copper oxide superconductors with focus on $YBa_2Cu_3O_{7-\delta}$ is given, followed by the coverage of essentials of complex oxide thin film deposition technology with the copper oxides at its core. Here, the major physical vapor deposition technologies (evaporation and oxide molecular beam technology, sputtering and pulsed laser deposition) are described followed by an overview of substrate requirements to deposit high quality thin films. Opportunities by choosing special substrates with unique properties far beyond the usual mechanical support for a film are introduced with examples aside from usual lattice mismatch induced strain effects. One is the continuous modification of the strain state by poling ferroelectric oxide substrates linked to a piezoelectric effect, the other is the nanoscale tailoring of substrate step-and-terrace structures resulting in a controllable generation of planar defects in complex oxides, thus contributing to the physics of flux-line pinning in cuprate superconductors. In the second part of this review, first some highlights of single layer thin film research are given such as to tailor thin film orientation, generating well defined antiphase boundaries in $YBa_2Cu_3O_{7-\delta}$ thin films as flux-line pinning centers as well as contributions to understand fluctuation conductivity in relation to the pseudogap state. In the last section new developments in high T_c cuprate based heterostructures and superlattices are reviewed with a special focus on the opportunities offered by interface-induced electronic interactions.

PACS: **74.72.–h** Cuprate superconductors;
74.25.–q Properties of superconductors;
74.78.–w Superconducting films and low-dimensional structures.

Keywords: high temperature superconductor, high temperature superconducing thin films, multilayers and superlattices, complex oxide thin film preparation.

Contents

1. Introduction

1.1. The road to copper-oxide based high temperature superconductors

In the decades after the discovery of superconductivity (SC) by Kammerlingh–Onnes in Hg with a critical temperature, T_c, of 4.2 K, — excellently described in the Physics Today article by van Delft and Kess [1] — SC has been a challenging central topic in condensed matter physics. Superconductivity shows the fundamental property of the occurrence of vanishing dc-resistivity and the expulsion of weak magnetic fields (Meissner–Ochsenfeld effect). The field expulsion holds up to the thermodynamic critical field, H_c, (type-I superconductors) and for type-II superconductors with a gradual decrease up to the upper critical field, H_{c2}. The vanishing resistivity holds up to a certain current density, called critical current, j_c. SC has application perspectives in a wide field of active and passive devices, cables, resonators, current fault limiters, just to name a few. The roadblock for a widespread application of SC was seen in the relatively low T_c's (< 10 K) and low critical fields (< 1 T, e.g., for Nb and V). Consequently, the quest for robust materials with higher T_c's and j_c's has been a driving force for materials scientists consisting in the empirical search for appropriate metal-based alloys. B. Matthias compiled the results of this research in his famous 4 rules for finding new superconductors as described in the monograph by Blundell [2]:

1. Transition metals are better than simple metals.
2. Peaks of density of states at the Fermi level are helpful.
3. High crystallographic symmetry is good: Cubic is best.
4. Stay away from oxygen, magnetism, and insulating phases.

Albeit these empirical rules had been very helpful in designing conventional superconducting materials, they failed in paving the way to the discovery of new families of superconductors more appropriate for practical applications. Additionally, during the time span until the early 50's, a theoretical guideline for a systematic search for better materials was missing completely. Deviating from his rules, however, Matthias found a new class of superconductors by combining ferromagnetic and semiconducting elements in $CoSi_2$ with a T_c of 1.33 K [3] indicating the openness required in the search for a new domain of superconducting materials. SC has been seen till the early 60's last century more as a scientific curiosity with a bright application potential rather than being useful for applications. This situation changed 1962, when Berlincourt and Hake discovered high critical currents in Nb–Ti alloys with a T_c of 10 K and a H_{c2} of 10 T [4], materials suitable for magnetic coil fabrication. 1952 Hulm and Hardy [5] discovered superconductivity in the "A-15" (β–W structure) family where in the A_3B structure the A site is typically occupied by a group VA transition metal (e.g., V, Nb, Ta) and the B site is occupied by a group IVB element (e.g. Sn, Ge, Si). Matthias and coworkers produced ~ 30 A-15 compounds by bulk preparation techniques mostly in thermodynamic

equilibrium, all of them with T_c's below 20 K. A breakthrough achieved Gavaler by synthesizing stoichiometric A-15 materials by thin film sputtering techniques and found in the thermodynamically metastable Nb_3Ge a record T_c of 23 K and an upper critical field of 37 T [6]. It is interesting to note that the highest T_c of all A-15 compounds is the thermodynamically metastable Nb_3Ge with pronounced peaks in the density of states (DOS) at the Fermi level, E_F. Systematic variations of the preparation conditions for Nb_3Ge thin film growth, e.g., revealed a distinct correlation of lattice defects (mainly in the Nb-chains of the structure) and the physical properties of the films [7]. Attempts to enhance T_c in A-15 compounds, e.g. by substitution of Ge by Si with an expected reduction of the lattice parameter and thus a $T_c > 30$ K failed.

In the early 1950's, the T_c, of the superconductors was shown to be sensitive to the isotopic mass of the constituent elements, pointing towards a role of phonons in superconductivity [8]. This observation led to the major theoretical breakthrough in 1957 when a microscopic theory of superconductivity was introduced by Bardeen, Cooper and Schrieffer (BCS theory), which described quite well the essentials of SC in metallic elements and alloys [9]. The BCS theory has two main conceptual ingredients, first, the pairing of electrons into Cooper pairs consisting of two electrons near the Fermi surface with opposite spins and momenta, glued together by lattice vibration of ions and second, their phase coherence. This theory served as a guideline for the search for higher T_c's highlighting the essential role of electron–phonon coupling and the high DOS at E_F. In the following decades progress in SC was made in several directions. One was the investigation of magnetic properties of superconductors by introducing the concept of flux-lines [10] and flux-line pinning to enhance the current-carrying capability, thus leading to large scale applications such as wires, cables and superconducting magnets, the other one in developing passive (microwave) and active (digital) devices based on thin film technologies. The third one was the further development of the BCS concept of electron–phonon coupling by Eliashberg [11] especially for the strong coupling case. Efforts to further enhance T_c have not been successful, on the contrary, is was believed that the maximum T_c is confined to values < 30 K mainly due to lattice instabilities.

In 1986, J.G. Bednorz and K.A. Müller discovered superconductivity in the ceramic La–Ba–Cu–O copper oxide with a T_c of about 35 K [12], which is considered to be a landmark event and represents the beginning of the field of high temperature superconductivity [HTS]. Their search for new superconductors was stimulated by the ideas of Jahn–Teller based polaronic effects associated with the polarizability of oxygen in the perovskite structure. Müller regarded that to be of major importance for the formation of Cooper pairs and thus superconductivity. It turned out that this concept of polarons (or bipolarons) being relevant to the origin of HTS experienced a strong opposition from the community relating HTS to strong electron correlation mechanisms [13]. The discovery of $La_{2-x}Ba_xCuO_4$ was a breakthrough in the field of superconductivity and was followed by avalanche-like research activities culminating in a "Woodstock"-type meeting of the American Physical Society, 1987, and the excitement to publish research results in newspapers prior to serious peer-reviewed scientific journals. Whereas in the $La_{2-x}Ba_xCuO_4$ system one CuO_2 plane is embedded in between of (La,Ba)-O blocks regarded as a charge reservoir, Wu *et al*. found 1987 a multiphase Y–Ba–Cu–O cuprate system to be superconducting at 93 K (i.e., well above 77 K the boiling temperature of liquid nitrogen) [14]. The superconducting phase in the Y–Ba–Cu–O system was identified as $YBa_2Cu_3O_{7-\delta}$ (YBCO), a layered structure with 2 CuO_2 planes and Cu–O chains as the dominant structural elements. (c.f. Fig. 1).

Since then, different structural and physical properties of cuprates have been studied in detail, and to raise the T_c for these materials, cation substitution has been extensively investigated. Since cuprate SC's with one CuO_2 plane show T_c's of ~ 35 K those with 2 CuO_2 planes ~ 92 K and with three planes ~ 134 K attempts to synthesize materials with more than 3 CuO_2 planes have been made, with no success, however. At present the highest T_c of 134 K is found in the three layer mercury-cuprate system ($HgBa_2Ca_2Cu_3O_{8+x}$) with an increase to 150 K under high pressure conditions

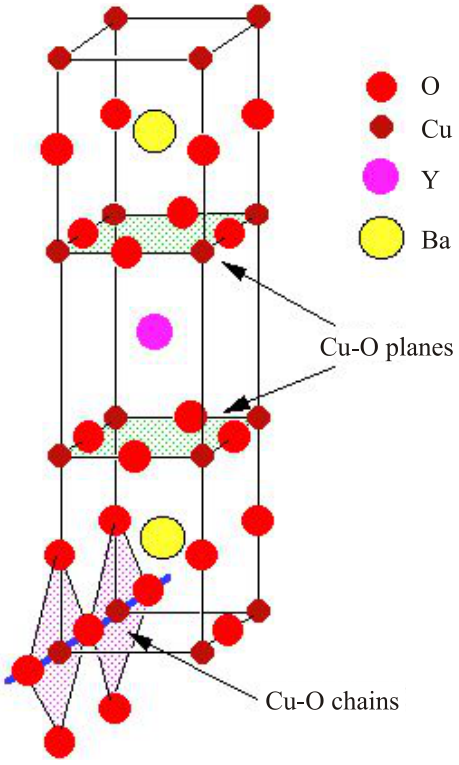

Fig. 1. (Color online) Unit cell of YBCO indicating the CuO_2 planes (with Cu (2), O (2) and O (3) atoms) and CuO chains (with Cu (1) and O (1) atoms) (after Wikipedia).

[15]. The cuprate high T_c superconductors identified so far have CuO_2 square planes as structural elements in common, outside this plane the structural elements serving as charge reservoir can be quite different thus causing the wide spread of T_c's in the copper oxides. After the discovery of superconductivity in La–Ba–Cu–O and especially YBCO, the research activities followed two main directions. The first is more materials oriented with the focus on achieving higher T_c's, investigating the flux-line properties and understanding the mechanisms of flux-line pinning as well as technological work in fabricating materials as bulk samples, tapes, wires and thin films for practical applications. Here, large scale applications such as cables for power transmission and magnetic coil technology are envisaged as well as developing a reliable thin film technology for passive (filters, antennae) and active devices (sensors, Josephson junctions for digital applications). The proceedings of the Applied Superconductivity Conferences (ASC) as well as the European Conference on Applied Superconductivity (EUCAS) may serve as reference source in this area [16,17]. The other direction is dedicated to the understanding of the origin of superconductivity in the cuprate system with emphasis on research on the pairing mechanism. In the nearly three decades since the discovery of superconductivity in the copper oxides much knowledge has been accumulated about novelties of quantum matter, but despite of all the efforts up to now no generally accepted theoretical model to explain the origin of superconductivity in copper oxides emerged. In a recent review Keimer *et al*. [18] stated that a qualitative understanding of the nature of the superconducting state itself has been achieved. Unresolved issues include the astonishing complexity of the phase diagram, the unprecedented prominence of various forms of collective fluctuations, and the simplicity and insensitivity to material details of the "normal" state at elevated temperatures.

1.2. Basic properties of $YBa_2Cu_3O_{7-\delta}$

Yttrium–Barium–Copper oxide, $YBa_2Cu_3O_{7-\delta}$ is the most frequently investigated member of the family of copper-oxide superconductors and serves as a prototype material for this class of materials. Its key properties are described in this section.

1.2.1. Crystal structure

As shown in Fig. 1, YBCO has a layered structure which can be described as a distorted, oxygen deficient perovskite of the form ABO_3, tripled along the *c*-axis, where Y and Ba are central cations which are stacked in Ba–Y–Ba sequence in the *c*-axis and Cu is the corner cation B. Yttrium is coordinated to 8 oxygen atoms forming a square prism while Barium is coordinated to 10 oxygen atoms. The valence of Y and Ba are +3 and +2, respectively, while Cu has mixed valence of +2 or +3 to ensure charge neutrality. The structure of stoichiometric superconducting YBCO is orthorhombic belonging to P_{mmm} symmetry and characterized by two CuO_2 planes ((a), (b) planes) and Cu–O chains. Highly oxygen deficient non-superconducting $YBa_2Cu_3O_{7-\delta}$ with $\delta > 0.6$ has a tetragonal structure with $P_{4/mmm}$ symmetry due to the interrupted or missing Cu-O chains, in $YBa_2Cu_3O_6$ the chains are missing completely. Cu (1) is at the center of a rectangle formed by its coordination with two O(1) and two O(4) atoms, these rectangles are connected by the vertices and give rise to CuO chains along *b*-axis. Cu (2) is coordinated in the form of a square pyramid to two O (2) and two O (3) atoms in the (a), (b) plane and one O (4) atom along the *c*-axis [19]. CuO_2 planes formed by Cu (2), O (2), and O (3) atoms are extended infinitely in the specimen and are crucial to determine the transport and superconducting properties of the material. For $\delta = 0$, i.e., $YBa_2Cu_3O_7$ the oxygen sites along *a*-axis in the basal CuO chain plane are completely empty. With increasing δ, the one dimensional chains in the orthorhombic phase are disrupted by an increasing number of oxygen vacancies at the O (1) site along *b*-axis. All oxygen sites in the basal plane become empty for $\delta = 1$, i.e., $YBa_2Cu_3O_6$ [20].The lattice parameters for this material are $a = 0.3822$ nm, $b = 0.3891$ nm and $c = 1.1677$ nm making unit cell volume 3 times the standard perovskite cell [21].

1.2.2. Electronic phase diagram

Hole doped cuprates have a generic phase diagram of their phase evolution in terms of temperature vs the Cu valency (hole doping) as depicted in Fig. 2. The undoped parent compound with Cu^{2+} is an antiferromagnetic Mott insulator [22] which can be doped either by substituting trivalent cations with divalent ones as in the case of La_2CuO_4 or by oxygen filling the Cu–O chains as in YBCO. With increasing doping (corresponding to an increase of the oxygen valency), the antiferromagnetic tran-

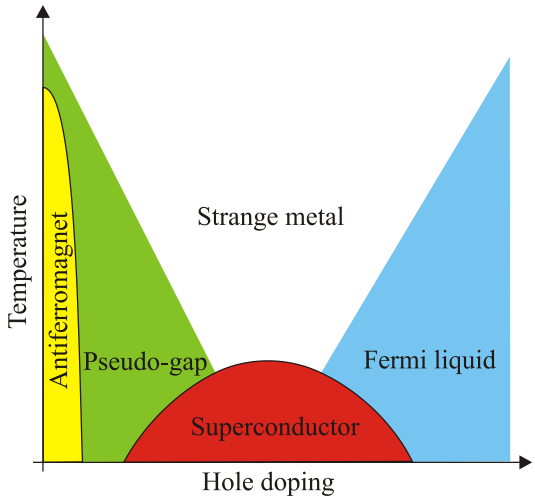

Fig. 2. (Color online) Schematic electronic phase diagram of cuprates [23].

sition temperature is rapidly suppressed and becomes zero; a further increase causes the superconducting state to emerge with low T_c at the beginning and gradually increases with the doping level (underdoped region), reaching a maximum at ~ 0.16 and then falls down gradually to zero (overdoped region) [23].

In the underdoped region above T_c, the normal state of cuprates is characterized by an intriguing feature called pseudogap which results in a depletion of the density of states. It was observed first in the NMR and inelastic neutron studies and was interpreted as a spin gap. Later ARPES, heat capacity and tunneling studies revealed that it is rather a gap in the spectrum of the quasiparticles. The exact origin of the pseudogap in cuprates is not yet clear, however the general scenario is that it arises from pairing fluctuations above T_c with no phase coherence, while in an alternative view pseudogap is a competing correlation that takes away the spectral weight that would be otherwise available for superconductivity. The pseudogap temperature specified in the phase diagram is not a sharp transition temperature but marks a gradual crossover into pseudogap region. In the overdoped region above T_c the conductivity of the copper oxides is smaller by nearly two orders of magnitude compared to usual metals and show a frequency and temperature dependence incompatible with the conventional transport theory of metals.

1.2.3. Superconducting properties

YBCO with a T_c = 92 K, is a highly anisotropic material based on the anisotropic crystal structure. It belongs to the Type II class of superconductors characterized by a large ($> 2^{-1/2}$) Ginzburg–Landau parameter $\kappa = \lambda/\xi$ with λ being the magnetic penetration depth and ξ the superconducting coherence length. Type II superconductors differ from type I superconductors, because in the latter the superconductivity is lost above a critical magnetic field H_c, whereas the former exhibits a complete Meissner state only below a lower critical field H_{c1}, above H_{c1} it shows a mixed state in which the magnetic field penetrates in the specimen in the form of flux filaments called vortices, arranged in a triangular lattice whose lattice constant decrease with field like $a \sim B^{-1/2}$ up to the upper critical field H_{c2}. For YBCO the upper critical field is about 150 T for magnetic fields applied parallel to the (a), (b)-planes and 40 T parallel to the *c*-axis. The superconducting gap in YBCO has a large value of about 30 meV which is much higher than any of conventional BCS superconductors with typical values below 1 meV. The superconducting gap in conventional metallic superconductors has *s*-wave symmetry around the Fermi surface, in the case of YBCO it has *d*-wave symmetry with nodes in different directions. The gap is zero in Cu–Cu direction whereas it maximizes along the Cu–O direction. The distance between two electrons of a Cooper pair is describe by BCS coherence length given by $\xi \sim v_F/k_BT_c$ and in conventional metal superconductors it is quite large, e.g. ξ = 37 nm for lead. Since T_c is 92 K in YBCO we can expect a small coherence length, however, due to the low density of carriers in cuprates, the Fermi velocity is also very small which makes coherence length even smaller such that ξ_{ab} = 1.5 nm and ξ_c = 0.2 nm [24]. YBCO is characterized by an electronic mass anisotropy, γ, causing ξ_c shorter than that of the basal plane by $\xi_c = \xi_{ab}/\gamma$. The extremely short coherence length poses some conceptual problem about pairing mechanism and determines the length scale for homogeneity requirements for the material. The penetration depth λ of a superconductor, which measures the distance to which magnetic field penetrates through a superconductor, is related to the superfluid density n_s by the relation $n_s \propto 1/\lambda^2$. For YBCO the penetration depth is very large with λ_{ab} (0) = 150 nm and λ_c (0) = 600 nm, consequently the superfluid density is relatively small. Due to the presence of Cu–O chains along *b*-axis, the coherence length is smaller compared to that along *a*-axis, the value λ_{ab} is calculated as $(\lambda_a \lambda_b)^{1/2}$.

The current carrying capacity, expressed as the critical current density, j_c, is an important figure of merit for a superconductor from potential applications' point of view. High values of j_c require the blocking of the motion of the Abrikosov vortices — nanoscale tubes of magnetic flux that form spontaneously inside a superconductor when exposed to a magnetic field larger than H_{c1} in the form of a triangular lattice. Their dimensions are determined by the coherence length, the corresponding supercurrents decay at a distance of λ. In general, j_c is a measure of the volume pinning force exerted to the vortex lattice. For layered cuprates j_c is very anisotropic. In case of YBCO, the value of j_c depends upon the nature of the specimen itself. For bulk specimens, e.g. single crystals, the j_c is pretty low ranging from 10–10^3 A/cm^2 , highest values are however obtained for epitaxial thin films of YBCO with $j_c \sim 10^7$ A/cm^2 at 77 K. Lower j_c values for bulk specimen arise mainly from intergrain weak links [25].

1.2.4. Current challenges in copper oxide science and technology

To improve and potentially surpass the superconducting properties of the existing copper oxide materials a fundamental comprehension of the essential principles underlying superconductivity in this class of materials is required. To achieve this goal several research challenges have to be met. One is seen in the understanding of the pairing mechanism — may be the interplay of several of them — that causes the formation of Cooper pairs, the other is the physics of the competing electronic phases especially in the pseudogap region. The investigation of the coupling of superconductivity with other competing electronic phases and their potential manipulation to improve their properties (T_c, j_c) is another big challenge. Currently, the theoretical methods available seem not to be adequate to describe the rich physics of the pseudogap phase and the region of the

strange metal behavior in the electronic phase diagram and much efforts are required to improve this situation.

Another cross-cutting challenge is more technology oriented. It is the further development and refinement of techniques to grow samples (single crystals, thin films, heterostructures and superlattices) with atomic precision and to improve existing diagnostic tools for the analysis down to the atomic level. These requirements arise from the fact, that the essential ingredients for superconductivity — Cooper pairs forming the superconducting state and Abrikosov vortices mediating the current-carrying capacity — have in the copper oxide superconductors dimensions in the nm range. The nanoscale interactions between themselves and crystallographic structures of comparable size determine their superconducting properties. Consequently, both, preparation methods and analytical tools have to take this basic feature into account and must meet the corresponding precision requirements.

2. Physics and technology aspects of high temperature superconductor thin film deposition

2.1. General aspects

Fabricating electronic devices and integrated circuits using superconductors requires a reliable thin film technology. In the case of low temperature metallic superconductors (LTS) this has been accomplished to a high degree of perfection by conventional techniques such as evaporation and sputtering and led, e.g., to optical and magnetic detectors with very high sensitivity [26]. Additionally, many efforts have been undertaken to fabricate digital integrated circuits; they have found so far niche applications, only [27]. Soon after the discovery of superconductivity in the copper oxides, the challenging task to develop a technology to prepare textured and single-crystal type thin films has been accomplished. The success in mastering the challenges has opened the door for research activities directed towards the fabrication of thin films, heterostructures and superlattices of other complex oxides such as manganites, ferroelectrics, and piezoelectrics. The availability of research-grade complex oxide thin film samples will further promote physics experiments directed to answer the basic questions of pairing mechanisms and current-carrying properties. By mastering the thin film technology for complex oxides, a new research field is arising using the opportunity to combine materials with different functionalities. An emerging topic is seen in the corresponding interface physics where contributions from the defect chemistry are mandatory to understand the interface properties. There is a long list of perovskite-type complex oxides with attractive physical properties which can be prepared as single-crystal type single layer thin films on lattice matched oxide substrates. Their application potential ranges from electrodes for solid oxide fuel cells to magnetic films for data recording/reading devices as well as superconducting thin film devices either of an active (SQUID basis) or passive (filters and antennae) type. The complex oxide thin film deposition technology is already covered by several review papers, conference proceedings and books [28–32]. This chapter does not aim to provide an exhaustive discussion of the physical processes behind film growth and deposition technologies, but focuses on the most relevant ones and the background for their relevance.

The key requirements for a mature technology suitable for applications are the ability to deposit single-crystal type layers and multilayer structures with the desired homogeneous chemical composition and nearly atomically flat surfaces. The length scale for inhomogeneities either structurally or morphologically is given by the short interaction lengths for the cooperative phenomena such as superconductivity and ferromagnetism in those materials. For superconducting cuprates, e.g., the coherence lengths along the *c*-axis is in the range of less than 1 nm [22]. The difficulties achieving such perfect complex oxide thin films (COTF's) are not only caused by the necessity to have the correct particle flux ratio of the constituents at the substrate site forming the correct crystal structure but also by the complex parameter space for the deposition of films with the desired crystallographic orientation and oxygenation state. This includes the deposition rate, kinetic energy of the particles impinging the substrate surface, substrate flatness and termination, and the thermodynamic requirements for phase stability as well. As an example the oxygen-pressure/temperature phase stability diagram for $YBa_2Cu_3O_{7-x}$ is given in Fig. 3. There are stability lines for the formation of the desired oxygenation state of Cu

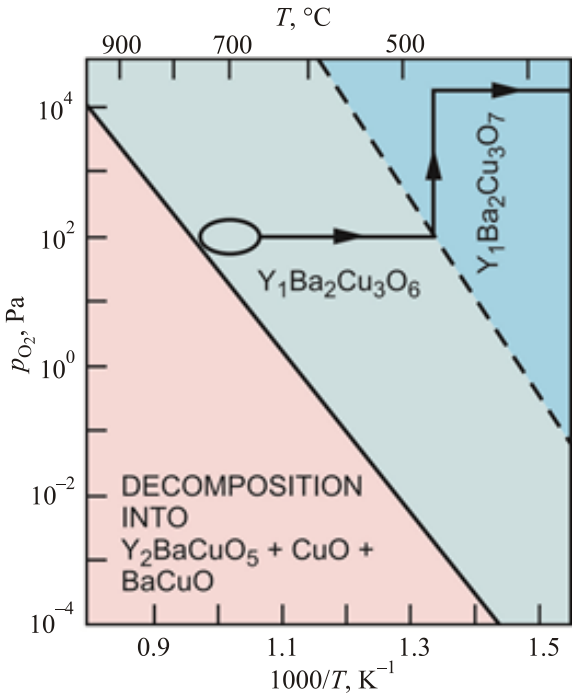

Fig. 3. (Color online) Phase stability diagram p_{O_2} vs $1/T$ for $YBa_2Cu_3O_7$ thin film deposition [31].

and the different levels of oxygen incorporation. Controlling the temperature and oxygen partial pressure independently during the cooling process it is possible to adjust the oxygen content of a film in a well-defined way. Within the parameter range set by the phase stability criteria, thermodynamic and kinetic factors determine the growth. The growth process of the films starts typically by the formation of a 2D nucleus with radius, r, and an edge free energy, γ, and is governed by the Gibbs free energy

$$G(r) = -\Delta\mu\pi r^2 h + 2\pi r\gamma h . \quad (1)$$

With $\Delta\mu$ being the excess chemical potential and h the height of the nucleus. For the formation of a heteroepitaxial nucleus a surface energy term for the interface has to be added. The nucleation and growth mode is governed by the relative supersaturation, p/p_{eq} — with p being the vapor pressure and p_{eq} the equilibrium vapor pressure at a certain temperature — as driving force for the film growth related to the excess chemical potential $\Delta\mu$ by

$$\Delta\mu = k_B T_s \ln(p/p_{eq}) . \quad (2)$$

The supersaturation has a strong influence on the growth mode of the films — either dislocation-controlled spiral growth (small supersaturation) or two-dimensional nucleation [island formation] up to a critical supersaturation $(p/p_{eq})^*$. Further increase of (p/p_{eq}) causes a transition to unstable growth, uncontrolled nucleation of growth centers on top of each others lead to a dendritic growth type [34].

In addition to supersaturation the deposition temperature, T_s, plays an important role in determining the growth kinetics and the surface morphology of the films. The relevant quantity is the normalized bonding energy, $E_b^{(i)}$, for the different species,

$$E_b^{(i)} = 4\Phi_{ss}^{(i)}/2k_B T_s \quad (3)$$

($\Phi_{ss}^{(i)}$ denote the potential energy of a solid-solid nearest neighbor pair of atoms in the substrate unit cell). It is obvious that increasing deposition temperature implies a smaller E_b causing a higher density of kink sites on the surface and a more rapid growth. For the spontaneous nucleation of a unit cell a critical volume of the deposited material is necessary. Since single atoms are impinging the substrate, diffusion is required to ensure that a nucleus has the appropriate constituents of the complex material to grow. The surface mobility of the particles impinging the substrate surface is one of the most important growth parameters. The adatom mean diffusion length, λ, is given by $\lambda = (D_s\tau)^{1/2}$ where D_s is the surface diffusion constant and τ the surface residence time. The diffusion coefficients for the different cations, however, can differ drastically; for YBCO e.g. they vary by 4 orders of magnitude from Y (10^{-13} m^2/s) to Cu (10^{-9} m^2/s) at a deposition temperature, T_s, of 800 °C. Consequently, the formation of nanoprecipitates and compositional phase separation is facilitated [35,36].

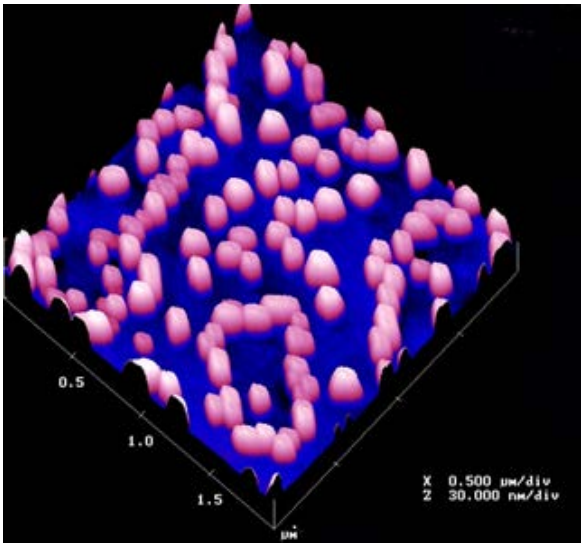

Fig. 4. (Color online) Nanodot-type surface of a 7.5 nm $La_{0.9}Sr_{0.1}MnO_3$ film deposited on a (100) $SrTiO_3$ substrate (taken from [31]).

STM studies of YBCO, e.g. grown by pulsed laser deposition on $SrTiO_3$ (STO), showed that the growth generally proceeds layer-by-layer followed by the formation of islands (multilevel 2-dimensional growth) [37]. In cases where epitaxial strain plays a role Stranski–Krastanov growth (islands on a wetting layer) occurs. Fig. 4 shows an example of an ultrathin (7.5 nm) $La_{0.9}Sr_{0.1}MnO_3$ film deposited onto a STO (001) substrate where dot-like features (diameter ~ 20 nm height ~ 7 nm) are formed on a 2 unit cell thick wetting layer [38]. Terashima *et al.* [39] directly proved the Stranski–Krastanov growth of YBCO by observing oscillations in the intensity of reflection high energy diffraction [RHEED] signals during film formation using reactive evaporation techniques. The oscillations in reflectivity are inferred to be the complete unit cell of the oxide. Compared to the layer-by-layer growth of semiconductor heterointerfaces, controlled by the highly directional covalent bond of the constituents, the growth of COTF's and consequently their film properties are governed by the constraint of preserving charge neutrality and stoichiometry imposed by the ionic character of the bonds. The minimum growth unit is thus a complete unit cell [40]. This opens the opportunity to grow heterostructures and superlattices of complex oxides with atomically sharp interfaces and basically no interdiffusion and antisite defects across the interface.

2.2. Substrate requirements and opportunities

For the development of a reliable deposition technology for high-quality COTF's, the choice of the substrate material is of primary importance. A review of substrates suitable for complex oxide thin film deposition with emphasis

on substrates for high temperature superconductors for microwave circuit applications is given by Hollmann *et al*. [41]. Following Wördenweber [28], the optimal substrate has to meet the following conditions:

a) crystallographic lattice match between film and substrate to avoid strain-induced defect generation,

b) similar thermal expansion coefficients of film and substrate,

c) no chemical interaction at the interface between film and substrate,

d) atomically flat polished surfaces, structurally as well as chemically stable.

Generally we can distinguish between two classes of substrates: (i) those compatible with the oxide thin film deposition technique without additional buffer layers and (ii) those where a buffer layer is required to accommodate large lattice mismatch or to prevent chemical interaction between substrate and oxide thin film. Typical candidates of the first category are $LaAlO_3$, $SrTiO_3$ and MgO for cuprate and manganite thin film deposition. In Table 1 some of the most frequently used substrates and their properties are listed.

Substrates are much more than merely a chemically inert mechanical support for thin films; they are functional elements in thin film technology [42]. On the one side, they can be prepared as chemically well terminated atomically flat surfaces at microscopic dimensions [43,44] on the other, intentional surface miscut and subsequent recrystallization (vicinal cut substrates) enables a nanoscale tailoring of step and terrace structures of the surface [45]. Figure 5 represents a TiO_2 terminated STO (001) substrate with large area atomically flat terraces interrupted by 1 unit cell high steps. The terrace width is determined by the unavoidable miscut of the substrate, which is determined in case of the Fig. 5 to be ~ 0.074^0.

Figure 6 shows the rather regular step- terrace structure of a STO (001) substrate with an intentional miscut of 1.2^0 towards the [010] direction. Depending on the terrace width, the growth mechanism of films using such substrates usually changes from the Stranski–Krastanov mode to the step-flow mode generating antiphase boundaries at the step edges if there is a mismatch of substrate and film unit cell height [45]. In the case of YBCO this causes anisotropic flux-line pinning and thus flux penetration [46] in case of ferromagnetic manganites a uniaxial anisotropy of the magnetic domain arrangements and an anisotropy of the hysteresis curves [47].

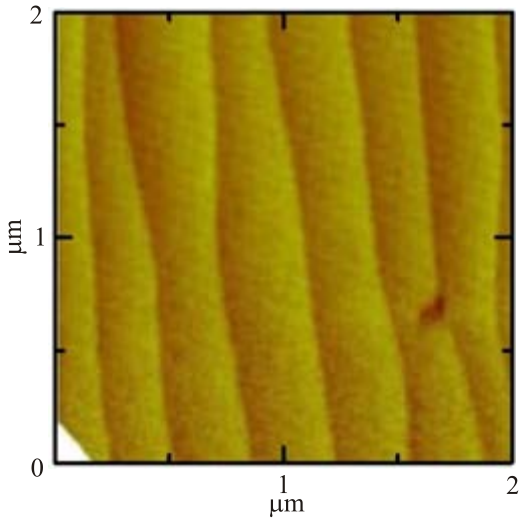

Fig. 5. (Color online) TiO_2 terminated $SrTiO_3$ surface showing large atomically flat surfaces (Courtesy of H.J. Kim, Max-Planck-Institute for Solid State Research Stuttgart, 2007).

Furthermore, controlled lattice mismatch can be used to tailor the biaxial in-plane strain states in the films and the relation to their physical properties. In the case of optimally doped bilayer copper oxides (e.g. YBCO) the primary superconducting properties (T_c, H_{c2}, j_c,) are found to be weakly strain dependent. Pahlke *et al.* determined the shift of the superconducting transition temperature to about 0.75 K per 1% compressive biaxial strain for optimally doped YBCO, whereas a significantly higher strain sensitivity of 4.20 K per 1% strain was found for underdoped YBCO [48]. For single layer cuprates (e.g. $La_{1.9}Sr_{0.1}CuO_4$) Locquet *et al*. could achieve a doubling of T_c by compressive strain [49]. It is believed, that the lattice deformations associated with the strain fundamentally modify the energy scales, leading to the formation and condensation of the Cooper pairs with consequences for the properties of the normal state. In other complex oxides, too, the strain state can substantially affect phase transitions and transport properties. Razavi *et al.* [50]

Table 1. Properties of substrates suitable for thin film deposition of complex oxides

Material	Thermal expansion coefficient (10^{-6})	Melting temperature, °C	Misfit to YBCO, %	Twinning	Chemical stability
$NdGaO_3$	9–11	1670	0.04	no	good
$LaSrGaO_3$	10	1520	0.26	no	good
$SrTiO_3$	9.4	2090	1.4	no	good
YSZ	11.4	2550	6	no	good
MgO	14	2825	9	no	good
$LaAlO_3$	10	2100	–2	yes	good
$LaSrAlO_3$	7.55	1650	–2.6	no	good

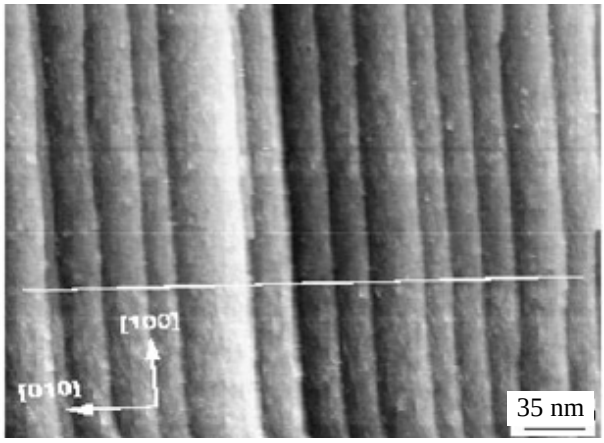

Fig. 6. Step-and-terrace structure of a TiO_2 terminated $SrTiO_3$ substrate with an intentional miscut of 1.20 vs [010] (taken from Haage *et al*. [46].

could convert the antiferromagnetic insulating state of $La_{0.1}Sr_{0.1}MnO_3$ into a ferromagnetic metallic one by compressive in-plane strain. Here, epitaxial strain compression of the lattice by the substrate enhances the lattice stiffness, and consequently the Debye temperature, Θ_D. The enhancement of Θ_D causes a reduction of the static Jahn–Teller distortion and an increase of the double exchange interaction Mn^{3+}–O–Mn^{4+}. The group around D. Schlom explored the possibility of adjusting the ferroelectric (FE) transition temperature, T_{FE}, by strain [51]. They could show that for heteroepitaxially grown $SrTiO_3$ films deposited on $DyScO_3$, tensile epitaxial strain causes an increase of T_{FE} by hundreds of degrees and produce room-temperature ferroelectricity in strontium titanate, a material that normally is not ferroelectric at any temperature. This strain-induced enhancement in an ordering temperature is the largest ever reported.

A further sophistication of the opportunities offered by dedicated substrates is seen in piezoelectric substrates where the in plane lattice constant of the substrate can be continuously changed by ferroelectric poling and the inverse piezoelectric effect linked with it. To study strain effects in complex oxide thin films, conventionally films of nominally identical thicknesses are prepared using identical deposition conditions on substrates with different lattice parameters. This approach implies that extrinsic variables such as substrate surface quality, film microstructure and oxygen stoichiometry are identical. An elegant way to circumvent these problems and focus on the strain state only, is the application of the converse piezoelectric effect by poling ferroelectric substrates. This is accomplished by reversibly compressing the isotropic in-plane lattice parameter of the rhombohedral piezoelectric (0.67[$Pb(Mg_{1/3}Nb_{2/3})O_3$]-0.33[$PbTiO_3$]) (001) substrates by application of an electric field $E < 12$ kV·cm^{-1} yielding an in-plane change of the lattice parameter < 0.12%. The application of PMN–PT single crystals has shown to be promising [52,53]. Depending on the polarity of the applied voltage, compressive or tensile strain can be achieved. Applying ac-voltage dynamical processes can be realized (c.f. Fig. 7).

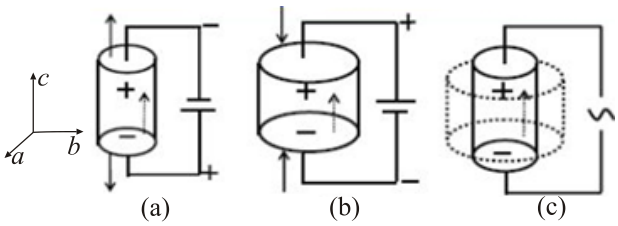

Fig. 7. Principle of the poling experiment.

In a practical example Zheng *et al*. [54] tested these concepts using PMN–PT single crystals as ferroelectric substrates and $LaMnO_3$ as well as $CaMnO_3$ thin films and observed a strong coupling of the Jahn–Teller distortion to the charge carriers. In Fig. 8 the principle of the experimental set-up is shown and in Fig. 9 the results for sputtered $LaMnO_{3-\delta}$ films are given. The data clearly show that poling of the ferroelectric substrate curtail a reduction of the in-plane tensile strain in $LaMnO_{3-\delta}$ films, thus weakening the electron-lattice coupling and generating a decrease of the resistivity and increase of the Curie temperature.

In general, using substrates as functional elements in the thin film technology of complex oxides, a rich opportunity is offered to tune their properties. They represent a possibility to investigate details of the structure-property relationship in complex oxide thin films. Strain generation and relaxation research can contribute to shed light on the intrinsic properties of these materials. Controlled modifications of the substrate surfaces are seen as a tool to study details of the film growth mechanisms and generate defect structures manageably.

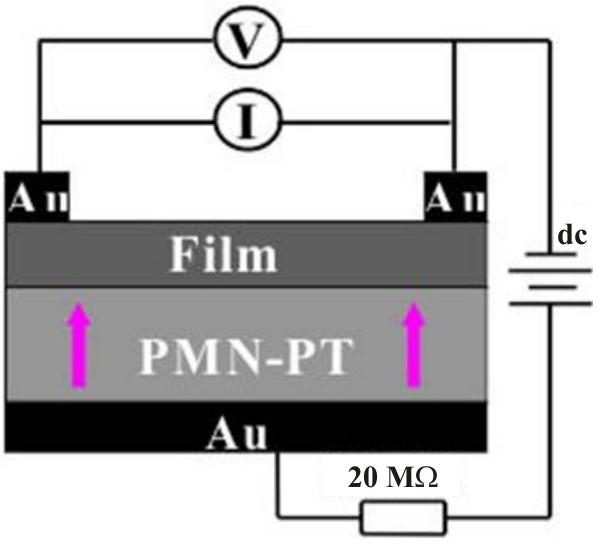

Fig. 8. (Color online) Sketch of the ferroelectric poling measurement [54].

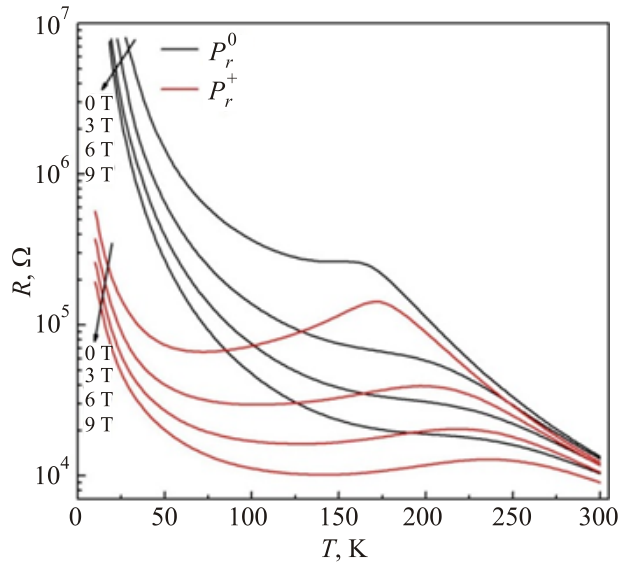

Fig. 9. Magnetic field dependence of the ferroelectric poling induced reduction in resistance of a $LaMnO_{3-\delta}$ thin film [54].

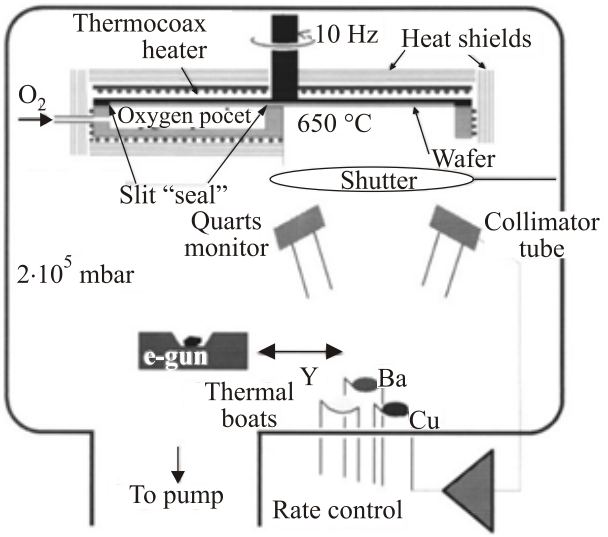

Fig. 10. Schematic sketch of a thermal co-evaporation system introduced by Utz *et al*. [56] with an oxidation pocket enclosing a part of the heater. The substrates are mounted on a rotatable disk moving continuously through the pocket.

2.3. Physical vapor deposition techniques for cuprates and other complex oxides

2.3.1. General remarks

Nearly all commonly used thin film deposition techniques have been more or less successfully employed for COTF thin film and multilayer fabrication, e.g. thermal and e-beam evaporation or co-evaporation, thermal or laser molecular beam epitaxy (MBE), on-axis and off-axis high-pressure sputtering, on-axis and off-axis pulsed laser deposition. While the *in-situ* deposition route (deposition and subsequent annealing/oxygenation in one chamber) is commonly used for most of the complex oxides, the *ex situ* routes (deposition of a precursor with subsequent treatment outside of the growth chamber) are applied, if one component forms volatile oxides at deposition conditions (e.g. TlBaCaCuO and HgBaCaCuO [55] film deposition).

In-situ deposition techniques usually use two steps, i.e. the deposition at high temperature (substrate temperature and oxygen partial pressure during deposition determined by the phase stability diagram) followed by a post-deposition oxygen treatment for the desired oxygenation and improved crystallization. For all deposition techniques, e.g. for copper oxides, three criteria must be fulfilled — at least when it comes to epitaxial films. (i) Since 3 or more cations are present, a precise tuning of their stoichiometry must be accomplished to avoid undesired foreign phases, (ii) a strong oxidizing environment must be ensured to get the Cu into the desired oxidation state and (iii) off-stoichiometry of the oxygen has to be avoided to prevent a degradation of the superconducting properties.

The description of the deposition techniques in this part is confined to the superconducting complex oxides of the rare earth (RE) RE–$Ba_2Cu_3O_{7-x}$ type which are considered to be the blueprint for other complex oxide materials.

2.3.2. Reactive evaporation

The most straight forward approach for YBCO thin film deposition is the application of co-deposition techniques using resistively heated boats or electron beam guns for high melting point metallic constituents combined with a rate control by quartz-crystal microbalances and computer-controlled tuning of the flux of evaporants. Reactive evaporation is an excellent technique especially to finely tune the composition of the individual layers and to grow large area films. One fundamental problem is the appropriate amount of reactive oxygen in conjunction with the requirement of the operation conditions for the e^--guns and the long mean free path of the evaporant. A very effective implementation of the evaporation technique has been realized by Utz *et al*. [56] utilizing a black-body-type rotating disk heater which had a deposition section and a oxidation pocket with a narrow opening so that in the oxidation section a relatively high oxygen pressure of 1 Pa can be maintained whereas in the chamber the background pressure is lower by a factor of 100 (see Fig. 10). Evaporation techniques require an accurate method of controlling the relative deposition rates of the constituents involved. This can be done by quartz crystal monitors, quadrupole mass-spectrometers or optical absorption measurements.

2.3.3. Oxide molecular beam epitaxy

Molecular-beam epitaxy (MBE) uses well-defined thermal beams of atoms or molecules which react at a crystalline surface to produce an epitaxial film. Originally developed for the growth of GaAs and (Ga,Al)As it is regarded now as a well matured growth technology for semiconductor Si and GaAs-type thin films, heterostruc-

tures and superlattices [57,58]. One reason for the big success of GaAs semiconductor MBE is seen in the adsorption controlled growth. Here, if sufficient As is supplied to saturate each Ga monolayer stoichiometric films grow, and the excess As desorbes from the surface and reenters the vapor phase. There is a wide growth window that eases the precision of the flux and temperature control requirement. MBE in general is a low kinetic energy deposition technique ($< 10^{-1}$ eV) thus avoiding a large concentration of defects (especially point defects) usually arising from high-energy species impinging the growing films. Epitaxial growth in a clean ultra-high vacuum deposition environment combined with in situ characterization during growth and the absence of highly energetic species are characteristic, distinguishing MBE from other deposition techniques. The transfer of this technology to complex oxides is a tremendous challenge. On the one hand this is due to the change from purely covalently bonded atoms in the semiconductors to the more ionically bonded charge reservoirs in the superconducting cuprates, on the other hand it is due the requirements of the appropriate oxygen supply to the growing film under MBE UHV conditions. The big advantage of techniques, reactive evaporation and oxide-MBE is the possibility to fine-tune the cation composition by an active composition control.

Due to the short length scale for inhomogeneities either structurally or morphologically, for all heterostructure and superlattice work one needs to deposit ultra-thin layers with interfaces as perfect as possible. Pioneered by Bozovic [59] and Schlom [60], reactive MBE has been demonstrated to be one of the most successful techniques to accomplish complex oxide film preparation with atomic precision. Reactive MBE being similar to reactive evaporation with the exception of a pressure range during deposition low enough to ensure a mean free path of the species emitted from the sources much longer than the source — substrate distance. Typical working pressures for reactive MBE are below 10^{-3} Pa. An advanced MBE system for complex oxide thin film work is depicted in Fig. 11. To provide molecular beams of the elemental constituents radiative heated effusion cells are used and the molecular beams are chopped by computer controlled mechanical shutters. The advantage of effusion cells over resistively heated boats is the more homogeneous momentum distribution of the evaporant impinging the substrate and the easier evaporant flux control. For successful atomic layer epitaxy it is necessary not only to monitor the relative ratios of the molecular beams of the different constituents but also the relative fluxes of the beams. Spectroscopic techniques such as atomic absorption spectroscopy are applied in addition to conventional quartz-crystal monitors. Modern MBE systems for complex oxide thin film research combine flux-controlled deposition from up to ten effusion cells with sophisticated *in-situ* analytical tools such as low energy electron microscopy [LEEM]/photo emission electron microscopy [PEEM], low energy electron diffraction [LEED] and time of flight ion scattering and recoil spectroscopy [TOF–ISARS]. The reactive MBE technique represents the most elegant and clean — however most costly — technique for COTF fabrication. Oxide MBE allows to further explore the layer-by-layer deposition process to prove the principles of the atomic layer engineering (ALE) of new metastable layered oxide compounds with in-situ RHEED control.

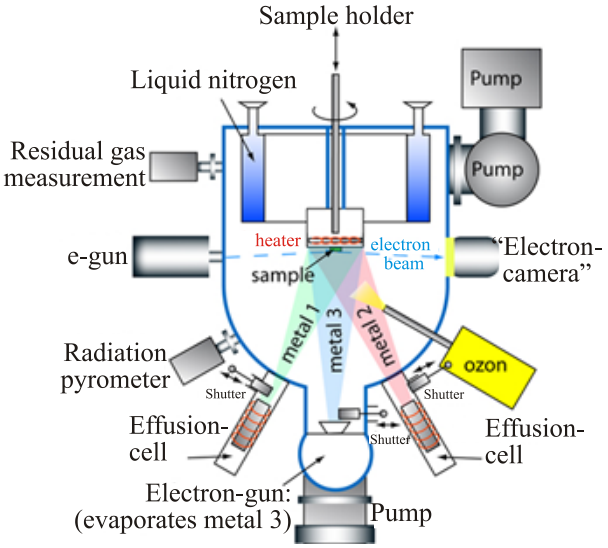

Fig. 11. (Color online) Sketch of a state-of the-art oxide MBE system as installed at the MPI-FKF Stuttgart. (Courtesy of G. Logvenov).

2.3.4. Sputtering

Sputtering — often described as playing billiard with atoms — is the ejection of target atoms as a result of bombardment by ions from a persistent glow discharge. It is a routine technique for numerous industrial applications and offers a possibility to quickly produce large area thin films even on curved substrates. The process relies on the production of plasma via an electrical discharge and the acceleration of ions (typically Ar^+) towards a target of the material to be deposited used as a cathode. The kinetic energy of the accelerated Ar^+ ions is usually in the range of 10–1000 eV. By a knock-on process on the target its material is ejected. In Fig. 12 the scheme of a sputtering system is depicted.

Reviews covering the basics of the physical processes in sputtering are given by Rossnagel [61] and Willmott [62]. It is a conventional widely used method where the film composition is normally expected to be equal to the target composition. As sputtering gas usually Ar is used, desired chemical reactions of the sputtered atoms/ions in the plasma can be achieved by adding reactive gases to the sputtering gas. In the case of multicomponent oxide systems tremendous problems arise from the formation of negatively charged particles at the target [cathode] side.

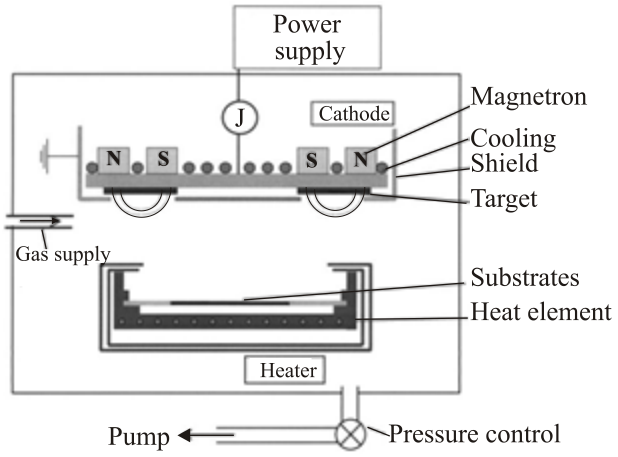

Fig. 12. Scheme of a sputtering system (after Wördenweber [28]).

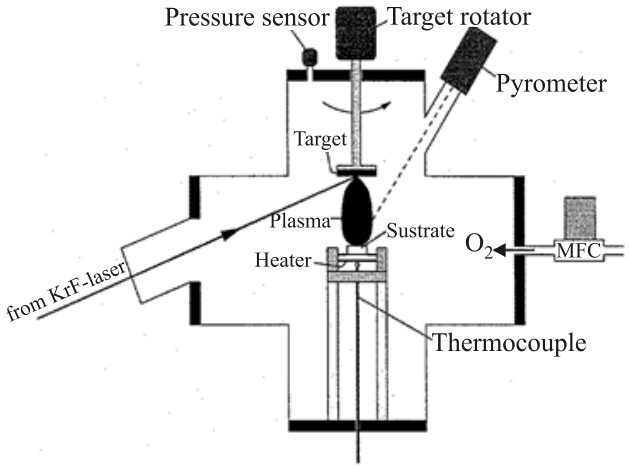

Fig. 13. Sketch of a typical PLD system.

Elements with a large electronegativity difference such as oxygen and the alkaline earth metals form negative ions which are accelerated away from the target by the potential difference of the cathode dark space. This energetic particle flux is directed to the substrate in conventional sputtering geometries leading to selective resputtering of the growing film which modifies the film composition or gives rise — in extreme cases — to etching of the substrate rather than film deposition. To overcome these problems at least four different routes are used: (i) to work at gas pressures high enough to reduce the kinetic energy of the ions striking the substrate below the binding energy [63], (ii) to place the substrate off-axis so it will not face the cathode. A very convincing realization of this idea is the inverted hollow cathode arrangement by Geerk [64], (iii) to design the system for a minimum discharge voltage [65] and (iv) to adjust the target composition for a compensation of the resputtering effects [66]. Practically, a huge variety of different arrangements of target — substrate position and target configurations have been applied or tried for *in situ* processes.

2.3.5. Pulsed laser deposition

Using pulsed laser deposition techniques short pulses – (typically 10–30 ns) of UV light are focused onto a target of desired composition. The light is absorbed according to its penetration depth and a thin layer of superheated material is formed which expands into the chamber in the form of a forward directed luminous laser plume. Figure 13 shows the principle of a pulsed laser deposition (PLD) system, schematically.

This technique, originally introduced by Dijkamp *et al.* [67] for the deposition of YBCO single layers has experienced a wide spread use for all kinds of oxide thin film deposition. A general description of the application potential of PLD and the chemical processes taking place during the ablation is given in the book of Bäuerle and references herein [68]. A review paper by Jackson and Palmer [69] discusses the operation of a laser deposition system and the influence of the operating parameters on the process. In brief, the PLD process consists of three parts: (i) the photon-target interaction, (ii) the plume formation and expansion and (iii) the film forming process at the substrate side.

The main features of the photon-target interaction, i.e. the high ablation rate, stoichiometric material transfer and the formation of a forward directed plume are usually described in a one-dimensional heat-flow equation.

$$\rho(T)c_p(T)\frac{\partial T(z,t)}{\partial t} = I(z,t)\alpha + \frac{\partial}{\partial t}\left(\kappa(T)\frac{\partial T}{\partial z}\right).$$

Here, c, κ and ρ are the heat capacity, thermal conductivity and resistivity of the target material, α is the absorption coefficient for the impinging photons. The power density of the laser light at the target surface is $I = I_0(1-R)$ with I_0 being the incident power density and R the reflectivity causes a depth profile $I(z,t)$ giving rise to a temperature profile $T(z,t)$ inside the target. Reaching the temperature threshold for vaporization, T_{th}, at the target surface a superheated sheath is formed and the vaporization process begins. Using a laser fluence of 0.4 J/cm^2 from a laser with 12 ns pulse duration Otsubo *et al.* [70] calculated the depth profile of $T(z)$ and found at a depth of 0.07 μm the maximum temperature of 2000 °C is reached in a YBCO target (absorption coefficient $2\cdot10^5$ cm^{-1}). When T_{th} is reached in the subsurface region the material will explode out of the target; the rapid speed of this process explains the nature of the congruent ablation of multicomponent materials and the feature of the highly directed plume of material above the target. The short time span for the material ejection and plume formation is the essential feature for congruent ablation due to the lack of time for segregation of the components of the plum according to their equilibrium vapor pressures which occurs by continuous heating, e.g. using electron guns.

The plume formation and expansion has been regarded already at early times of oxide-PLD as an essential part of

the deposition process including chemical reactions with the processing gas, pressure dependent particle velocity distribution, pressure gradients and material homogeneity within the plume. Its main features are the direction perpendicular to the target surface and the brightly colored material specific appearance. Dyer *et al.* [71] investigated the principal luminescent species, expansion velocities, and the extent of ionization using visible UV spectroscopy and ion probes. Their results have identified the major luminescent species in the plume of KrF laser ablated Y–Ba–Cu–O superconductor samples as arising from neutral and ionized atoms and suboxides. Relatively high temperatures appear to accompany ablation, resulting in high velocity emission (10^4 m/s) and corresponding particle energies in the 25–50 eV range. The extent of ionization in the plume is low ($S < 4\%$) for fluences up to ~ 4 J·cm^{-2}, i.e., neutral rather than ionized species will predominate in the deposition process under these conditions. Aruta *et al.* [72] performed extensive studies of plume properties and plume expansion using KrF laser photons during the ablation process of $LaAlO_3$ and $LaGaO_3$ by fast photography and space-resolved optical emission spectroscopy in an oxygen background pressure up to 10^{-1} mbar oxygen. They observed a strong dependence of the kinetic energies of the ablated species on the oxygen background pressure. For $p_{O_2} \sim 10^{-1}$ Pa the kinetic energy of La was determined to be 58 eV whereas in the case of $p_{O2} \sim 10$ Pa this value drops to 0.7 eV. This result indicates that the oxygen background pressure during ablation is a crucial parameter for the film forming process since the oxygen bond, e.g. to $SrTiO_3$, are in the order of 10 eV. This implies that at low oxygen pressures during ablation defect formation and oxygen vacancy generation is a complication to be considered in optimizing the PLD process.

Using typical deposition conditions for YBCO [T_D = = 760 °C, p_{O_2} = 20 Pa] growth rates of ~ 0.25 nm/s are achieved using a 5 Hz pulse repetition rate. Due to the stoichiometric ablation from the target it is quite simple to achieve chemical composition identity of target and film — provided no volatile species are formed. Heterostructures and superlattices can easily be prepared using this method. Computer-controlled target exchange systems are used and the individual layer thickness is defined by a separate growth rate determination. This is possible because the nominal thickness of the ablated material per pulse is much smaller as compared to the individual building blocks of the relevant oxide materials, simple pulse counting is sufficient for the thickness monitoring. This procedure however requires constant laser fluency per pulse which is dependent on the quality of the laser used. Systematic improvements of growth control can be achieved by the implementation of a differentially pumped Reflection High-Energy Electron Diffraction (RHEED) system suitable for operating pressures in the range of around 100 Pa [39]. The advantage of the PLD approach is its simplicity, flexibility and the possibility to switch from one material to the other just by replacing targets of typical sizes ~ 15 mm diameter and 5 mm thick. They can be fabricated in house usually, so new material combinations can be assessed quite quickly. The disadvantage of the PLD technique is seen in the restriction to small substrate areas of ~ 2 cm^2 and in the homogeneity of thickness and composition. Additionally, the high kinetic energies of the particles impinging the substrate [10–60 eV] can cause re-sputtering effects if the incident laser beam fluency is too high. The PLD approach is seen as an ideal low cost tool for exploratory research and development. In Fig. 14(a) (complete system) and 14(b) (inner part) a standard PLD system (DCA Finland) designed for heterostructure and superlattice thin film is shown, including the facility for a RHEED control of the growth process.

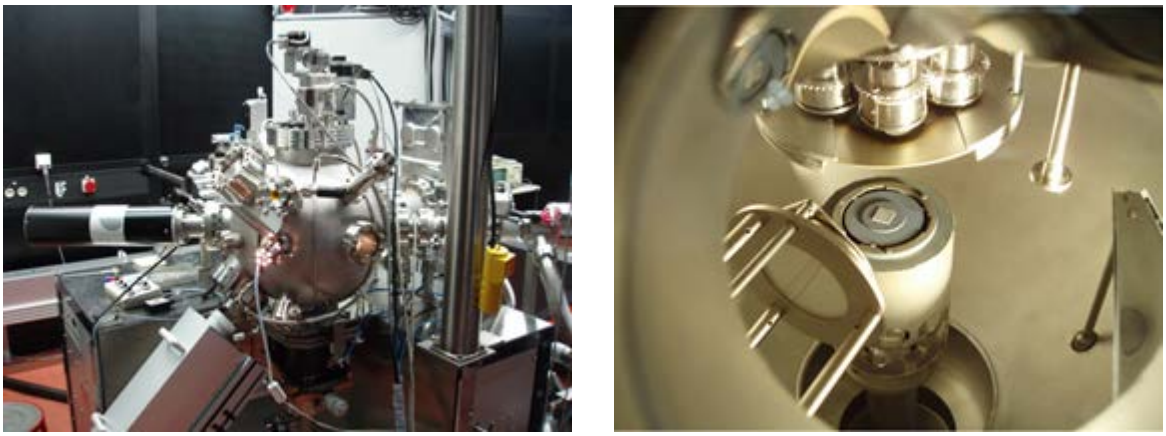

Fig. 14. (Color online) View of a UHV PLD system (DCA Finland) (left) and the inner part showing the target exchanger, sample heater assembly and RHEED screen (right).

Table 2. Comparison of the deposition techniqes

Method	Molecular beam epitaxy	Pulsed laser deposition	Sputtering
Superconducting properties (T_c, H_{c2}, j_c)	Excellent	Excellent	Fair
Composition control	QCM, AAS, EIES	Limited by process	Limited by target
Kinetic energy of particles at substrate, eV	10^{-2}–10^{-1}	1–60 Depending on the background pressure	2–10 Depending on the input power
Thickness control	Excellent	Excellent	Fair
Surface flatness	Good (if stoichiometric)	Good (but droplet problem)	Good
Ultra-thin film	Possible	Possible in optimized conditions	Poor
Large-area growth	Possible	Not achieved to satisfaction	Possible

2.3.6. Comparison of the different deposition techniques

Each of the in situ deposition techniques have their own advantages and disadvantages and different ultimate goals.

Whereas PLD techniques is the most flexible one and is capable to produce excellent single layer films, multilayers and superlattices, detailed parameter adjustments are necessary to avoid and/or minimize the droplet problem arising from the explosive character of the impact of the short pulse photons. One drawback, however, is seen in the thickness and compositional uniformity of the films limiting the useful size of a substrate to ~ 1×1 cm. Sputtering results in films of excellent quality suffers however from very slow deposition rates in the range of 20–100 nm/h. Evaporation and MBE techniques are scientifically the most rewarding ones due to the cleanliness of the process, the possibility of fine tuning the composition and the incorporation of in situ analytical tools. In Table 2 the advantages and disadvantages of the techniques are given schematically (after H. Yamamoto *et al.* in Ref. 32)

3. Physical properties of single layer high temperature superconductor thin films – some current trends

3.1. General remarks

In case of a successful accomplishment of a mature thin film technology to deposit single layer copper oxide thin films a plethora of opportunities to explore the fundamental properties of these materials is opened and the transfer of concepts for electronic devices developed for classical metal superconductors to their copper oxide counterparts is facilitated. In Fig. 15(a)–(c) typical results for a single layer YBCO film of 40 nm thickness are represented (x-ray diffraction pattern showing a purely *c*-axis oriented film (a) temperature dependence of resistance (b), and high resolution TEM (c) demonstrating the state-of-the-art quality of YBCO thin films. The technology has been developed to a high degree of perfection to address questions associated with the basics of high temperature superconductivity.

From the application point of view the materials issues are solved to the extent that Josephson-effect based devices (superconducting quantum interference devices–SQUIDS) for digital applications, passive devices such as microwave components, resonators etc. can be fabricated [16,17]. The main hurdle in accomplishing the technology transfer from low-T_c to high-T_c materials is seen in the extremely short coherence lengths of the cuprate superconductors (a few nm only) compared to the classical metallic ones (10s to 100s nm). Additionally, the *d*-wave symmetry of the order parameter as compared to the *s*-wave symmetry of the metals generates a further difficulty.

A comprehensive coverage of the field of active and passive electronic devices are beyond the scope of this paper, reviews can be found in the proceedings of the Applied Superconductivity Conferences (IEEE Transactions on Superconductivity), relevant reference books, e.g. [73], and review papers by Koelle *et al.* [74] and Newman *et al.* [75]. Here, only 2 more materials science related and one physics related examples are briefly described. One deals with the deliberate tailoring of the orientation of copper oxide thin films, with the *c*-axis either perpendicular or parallel to the substrate plane or tilted by 45° with respect to it. The second one describes the controlled generation of antiphase boundaries by nanoscale regular substrate surface patterning using the technique of substrates with a vicinal cut and to study details of flux pinning mechanisms by planar defects, and a third one covers properties of the potential of fluctuation conductivity measurements to shed some light on the physics of the pseudogap state.

3.2. Tailoring cuprate thin film orientation

Generally, superconducting copper oxide thin films grow with the crystallographic *c*-axis perpendicular to the substrate plane, i.e. the short coherence length is pointing perpendicular to the film plane. The driving force for this growth direction is seen in the different surface energies of the (100), (010) and (001) surface planes and the lattice match of, e.g., YBCO on $SrTiO_3$. Films of both types, *c*-axis aligned either perpendicular or parallel to the film plane are important for fundamental studies of the anisotropy transport properties of them as well as for potential applications, e.g., as planar Josephson junctions. Devices

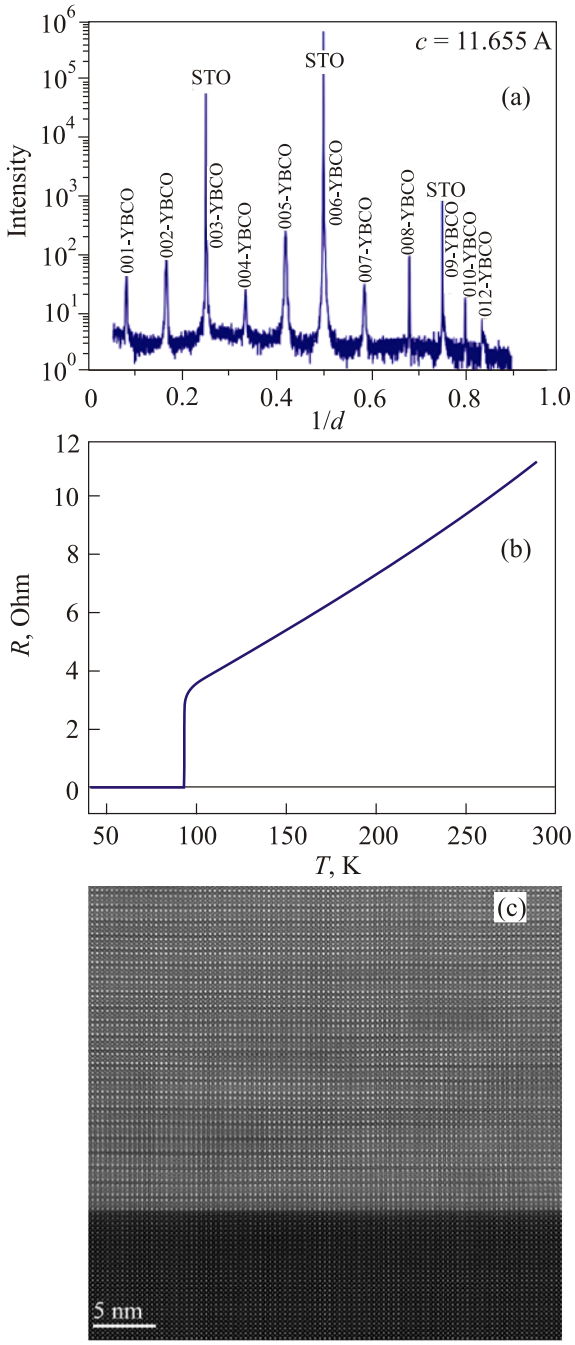

Fig. 15. (Color online) X-ray diffractogram of a 40 nm YBCO film deposited on a $SrTiO_3$ (100)-oriented substrate (a) corresponding resistance vs temperature plot (b). High resolution TEM of an YBCO film deposited on a $SrTiO_3$ (100)-oriented substrate showing the perfection of the film structure and the interface (c).

based on planar Josephson junctions should have the (a), (b) plane perpendicular to the substrate plane which is the case of (100) and (110) oriented films. In the late 80's several authors described the deposition of (110)-oriented YBCO thin films grown on (110) $SrTiO_3$ substrates [76,77]. Care must be taken that a dedicated film analysis is capable to distinguish between the (110) orientation and the competing $(103)/(10\bar{3})$ orientation with identical peak positions in the x-ray Θ–2Θ diffraction patterns. In Fig. 16 the two competing film orientations are displayed.

In addition to x-ray pole figures, Raman spectroscopy has been proven to be an elegant and fast tool to characterize high temperature superconductors as reviewed by Thomsen and Cardona [78]. Since the relative magnitudes and signs of the components of the Raman tensor (α_{ij}) for a given Raman mode are rather different for light polarized parallel or perpendicular to the CuO_2 planes, Raman scattering is an easy and fast method to determine the orientation and oxygenation of a single crystal or thin film.

Habermeier *et al.* [79] applied the $PrBa_2Cu_3O_{7-x}$ (PBCO) hetero-templating technique, where a $PrBa_2Cu_3O_{7-x}$ template of ~ 60 nm is deposited at a substrate temperature of 660 °C at an oxygen partial pressure of 1mbar followed by the YBCO deposition with continuously increasing the substrate temperature to 720 °C. The films show values for T_c between 83 K and 87 K. The corresponding x-ray diffraction pattern revealed almost single phase (110)-oriented films with the dominant diffraction peaks ascribed to the (110) and (220) reflections adjacent to the substrate (110) and (220) peaks. A weak indication of some *c*-axis grains could be identified, whose volume fraction was estimated to be less than 1/1000. Raman spectroscopy clearly revealed the (110) orientation as shown in Fig. 17.

$(103)/(10\bar{3})$ films can be grown using standard deposition conditions (T_s = 750 °C, p_{O_2} = 50 Pa) using (110)-oriented $SrTiO_3$ substrates. The $(10\bar{3})$ phase can be completely suppressed, if the substrate has an intentional miscut of 3.5° vs the [100] direction [80]. These films

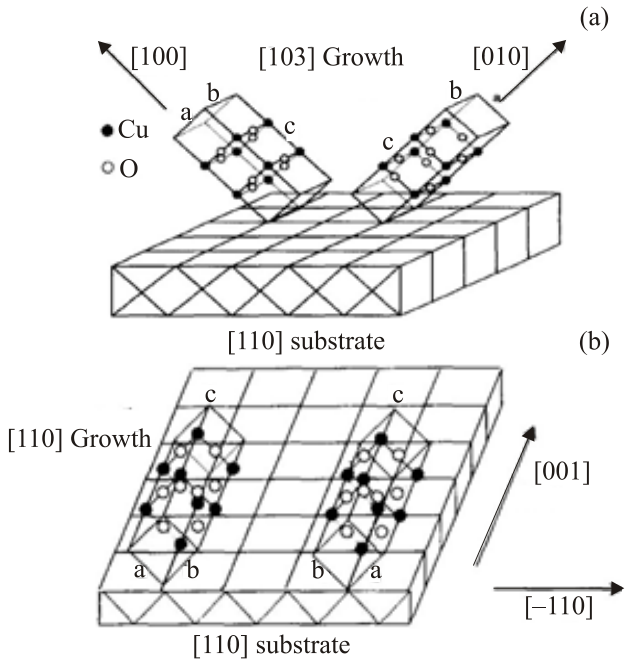

Fig. 16. Schematic representation of YBCO growth in $(103)/(10\bar{3})$ orientation (a) and (110)-orientation (b).

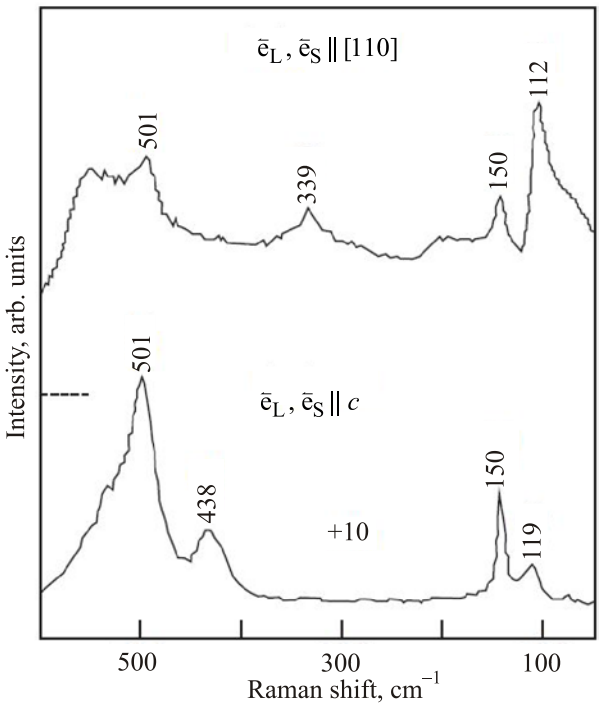

Fig. 17. Raman spectra of a (110) YBCO film. Lower spectrum: the laser beam propagating perpendicular to the film plane along [110], the incident and scattered light polarized along the *c*-axis lying in the plane. Upper spectrum: same direction of the laser beam but incident and scattered light polarized perpendicular to the *c*-direction along a (110) direction lying in the plane. [79].

show a slightly higher T_c and lower resistivity along the (a),(b)-plane compared to the (110) YBCO films indicating a lower defect density of the films.

The conclusion is that from the technological point of view detailed investigations of the anisotropy of the optical and transport properties are possible and the basis for fabricating planar Josephson junctions is accomplished.

3.3. Controlled generation of antiphase boundaries

As already mentioned, a current in a superconductor causes the Abrikosov vortices to move in a dissipative way unless they are pinned by defects. In general, the critical current, j_c, is a measure of the volume pinning force exerted to the flux-line lattice by extrinsic defects. The largest j_c's in YBCO of $3{\cdot}10^{11}$ A/m^2 at 5 K have been observed in epitaxial films with a high density of different lattice defects related to the Stranski–Krastaov growth of the films and the subsequent formation of grain boundaries. Since the microstructure is rather complex, much effort has been spent to identify the most effective pinning sites.

The concepts developed to treat flux pinning in classical superconductors are based on the analysis of the elementary pinning force, f_p, exerted to a single flux-line caused by a defect in the crystal lattice and the statistical summation of elementary pinning forces to an average volume pinning force, F_p. As one of the fundamental mechanisms leading to flux line pinning, suprastrictive interactions have been discussed. They are associated with stress fields around defects in an interaction volume determined by the superconductor coherence length and the dimension of the defect. The theoretical base of this concept is the phenomenological Ginzburg–Landau theory which gives a good description of the reality — at least in the vicinity of T_c, if the superconducting order parameter is only slowly varying within distances of the superconducting coherence length. This approach, however, cannot simply be transferred to the high temperature superconductors [HTS] mainly due to the fact of the extremely short anisotropic coherence length, ξ in the HTS materials with ξ_{ab} = 1.5 nm in $YBa_2Cu_3O_7$ in the CuO_2 plane and ξ_c = = 0.15 nm along the *c*-axis. Superimposed to the problems arising from the small values in ξ is the difficulty due to the poly-elemental composition of the material with a variety of possible lattice defects giving rise to a plethora of pinning mechanisms with — probably — quite different efficiency. In YBCO single crystals randomly distributed point defects such as oxygen vacancies lead to a weak collective pinning [81,82], correlated pinning has been demonstrated to arise from twin boundaries [83] and artificial columnar defects generated by heavy particle irradiation [84]. They allow the appropriate alignment of the vortex system with the defect structure resulting in higher pinning forces compared to collective pinning induced by point defects. In epitaxial thin films of YBCO the critical current, j_c, is generally at least one order of magnitude larger compared to twinned single crystals [85,86]. One dimensional defects such as screw dislocations [87], two dimensional defects like grain boundaries [88], precipitates [89] and surface roughness [90] had accounted for the strong pinning. Up to now it is not clear which of the different types of defects causes the higher j_c.

The growth controlled generation of an array of antiphase boundaries [APB's] leading to a planar defect structure and its effect on the transport properties of the films is one way to contribute to disentangle this complex situation. It is caused by the modification of thin film structure via growth on vicinal cut $SrTiO_3$ single crystal substrates. In Fig. 18(a) the formation of an APB at a substrate step is shown schematically.

Domains nucleating at adjacent terraces are shifted vertically by a fraction of a unit cell. Alternatively, a change of the stacking sequence on adjacent terraces enables a smooth and structurally defect free overgrowth of a substrate step. Figure 18(b) shows the antiphase boundary emerging from a STO surface step in an YBCO thin film. Combining UHV–STM investigations of the substrate in situ and film surface analysis after deposition in conjunction with transport and magneto-optical investigations, a more detailed analysis of these growth-induced pinning centers could be achieved [91]. In order to gain a more thorough understanding of the thin film growth and the

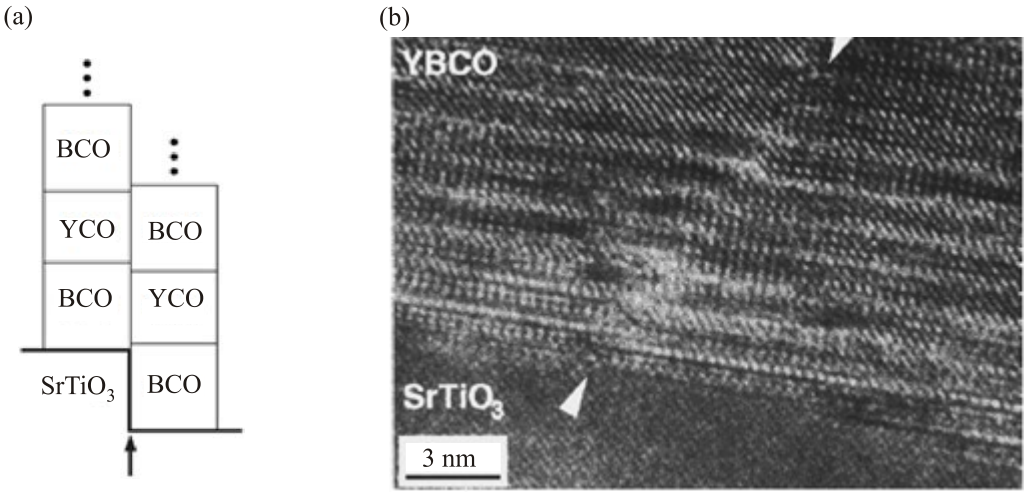

Fig. 18. Illustration of the formation of an antiphase boundary at a substrate step: domains nucleating on adjacent terraces are shifted vertically by a fraction of the unit cell (a); high-resolution cross-section TEM image showing an extended antiphase boundary (APB) marked by arrowheads (b) [46].

defect generation, the substrates and films were studied by UHV scanning tunneling microscopy (STM) in situ. Furthermore, this experiment may be regarded as a case study for the controlled generation of defects by intentional substrate modifications which is general in nature. It could be demonstrated, that pinning at growth induced planar APB's in YBCO thin films is dominated by quasiparticle scattering induced variation of the condensation energy. Crucial for this study of j_c in YBCO films is that the microstructure is dominated by only one kind of pinning site exhibiting strong correlated and anisotropic pinning. The combined study of magnitude, temperature and angular dependence of j_c with respect to the APB's plane by means of magneto-optics allows us to identify the pinning mechanisms. Microscopic theory [92] suggests two fundamentally different mechanisms giving rise to high pinning forces: (i) disorder induced spatial variation in T_c (δT_c pinning) and (ii) local variation of the quasiparticle mean free path l (δl pinning). In contrast to δT_c pinning, where defects of dimensions of at least the coherence length are required for effective pinning, the defect size for quasiparticle scattering pinning may be much smaller [92]. In superconductors with isotropic gap the δl effect influences only the kinetic energy of the supercurrent of a vortex. In the framework of collective pinning, Griessen *et al.* [93] interpreted their results as evidence for this pinning mechanism in YBCO thin films. Since then, the presence of an order parameter with $d_{x_2-y_2}$ or some mixed symmetry (s+d) has been established in YBCO [94]. In this case the Anderson theorem [95] is not applicable and elastic quasiparticle scattering breaks the Cooper pairs. Consequently, vortices interact with defects by the δl effect also via condensation energy. The results by Jooss *et al.* [96] prove this interaction mechanism of vortices at APB's in YBCO.

3.4. Fluctuation conductivity.

There is a general consensus that a complete understanding of the high T_c cuprate superconductors must include their normal state properties, especially in the range between T_c and the temperature where a pseudogap opens in the underdoped region of the generic phase diagram. As already mentioned, in this range the resistivity is nearly two orders of magnitude larger than in simple metals and shows frequency and temperature dependences that are incompatible with the conventional theory of metals; the regime above T_c is called the regime of 'strange metals'. The behavior is frequently described in terms of the so called "marginal-Fermi-liquid" phenomenology [97]. The structure of the pseudogap in momentum space can be directly analyzed by ARPES experiments and it formally mimics the d-wave superconducting gap. The pseudogap only appears in the antinodal direction of the Brillouin zone where the d-wave gap is largest. This experimental observation suggests that the pseudogap opens at a temperature where pairs already start to form. Phase fluctuations, however, prevent phase coherence and thus superconducting order. There are several experimental hints for the existence of these preformed pairs, a prominent strong one is the observation of diamagnetism [98]. Furthermore, a detailed analysis of fluctuation conductivity $\sigma'(T)$ can reveal a deeper insight in the pseudogap properties. Solovjov *et al.* [99] studied the fluctuation conductivity in YBCO thin films with controlled oxygen deficiency so the doping level could be tailored. The basic concept of this work is addressing the question of scattering due to the interaction with different types of excitations. One model is based on the resonant valence scenario of Anderson [100], here; the excitations are spinons and holons, which contribute to the resistivity. The holon contribution is assumed to be the governing one, whereas the spinons, which are efficiently coupled to the magnetic field H, should determine the temperature dependence of the Hall effect. The other models are based on the concept of anisotropy of the carrier scattering, arising from the complex band structure of the

cuprates or the influence of spin fluctuations. There are two fluctuation contributions to σ'(*T*). The direct contribution, which is given in a theoretical framework by Aslamazov and Larkin (AL) [101] arises as a result of the spontaneous formation of fluctuation-induced Cooper pairs above T_c. An additional contribution, introduced by Maki and Thompson (MT) [102] as an extension of the AL theory, is interpreted as being the result of an interaction of already existing fluctuating pairs with normal charge carriers and is governed by pair-breaking processes in the particular sample. The MT contribution depends on the lifetime τ_φ of the fluctuating pairs and is dominant in the region of two-dimensional fluctuations, whereas the AL mechanism dominates in three dimensional region of fluctuation conductivity near T_c. In layered structures, including HTSCs the AL contribution is usually described within the frame of the Lawrence–Doniach model [103], which predicts a smooth dimensional crossover from 2D to 3D fluctuation behavior for *T* approaching T_c. Solovjov's experiments show a clear MT–AL 2D to 3D dimensional crossover on the σ'(*T*) curves by reducing the temperature towards T_c as shown in Fig. 19.

Solovjov and Dmitriev reviewed the study of excess and fluctuation conductivity σ'(*T*) in $YBa_2Cu_3O_{7-y}$ and $Y_{1-x}Pr_xBa_2Cu_3O_{7-y}$ epitaxial thin films [104]. Their analysis is based on the idea that excess conductivity σ'(*T*) forms in HTSCs at temperatures substantially above critical temperature T_c as a result of the formation of pair states in the form of non-interacting strongly bound bosons, exhibiting with decreasing temperature a transition from a regime with localized pairs compatible with the Bose–Einstein condensation theory into a regime with fluctuation Cooper pairs which can be described within the frame of the BCS approach.

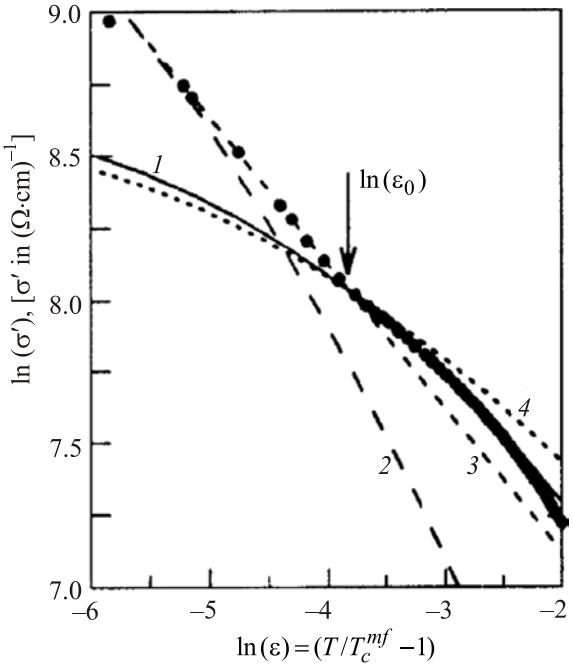

Fig. 19. Comparison of the experimental data of ln(σ') (full circles) vs ln(ε) with the fluctuation theories: curve *1* — MT contribution (scaling factor C_{2D} = 0.544, *d* = 1.17 nm), curve *2* — LD contribution (C_{3D} = 0.55, *d* = 1.17 nm), curve *3* — AL contribution (3*D*) (C_{3D} = 1), curve *4* — MT contribution (C_{2D} = = 0.494, *d* = 0.42 nm).

During the further development of complex oxide deposition technologies heterostructures and superlattices with antagonistic order parameters (e.g. superconductive and ferromagnet ones) could be synthesized and fluctuation conductivity measurements give rise to more insight on the interrelation of phase fluctuations, preformed pairs and dimensionality.

4. Complex oxide heterostructures and superlattices based on superconducting cuprates

4.1. General remarks

The technological advances in the atomic-scale synthesis of complex oxide heterostructures have provided a flourishing ground to explore electronic interactions either at their interfaces or across the layers in analogy to the mechanisms giving rise to the GMR effect in magnetic multilayers. In several recent review papers Hwang *et al.* [105], Keimer *et al.* [18] and Mannhart *et al.* [106] highlighted the fundamental physics background emerging from the breakthroughs based on advanced oxide thin film technology. In contrast to bulk materials, different symmetry constraints can be artificially imposed at the interfaces and thus offer the opportunity to design structures exhibiting new phenomena with potentially intriguing novel properties. Arising from the experimental results of generating conducting layers between oxide band insulators [107] and the analysis of cuprate/manganite heterostructures and superlattices [108], the concept of reconstruction of the charge, spin and orbital states at interfaces at the nanometer scale turns out to be a new research topic with strong impact on fundamental physics and possible applications as well. Interface superconductivity, magnetoelectric coupling, and the quantum Hall effect in oxide heterostructures are representative examples of the scientific and technological achievements in this rapidly growing field. Common to all these activities is the participation of at least one transition metal ion with the potential of occurring in different valence states.

Transition metal oxides (TMOs) are at the core of these research activities and are the ideal playground for the study of electron correlations. The transition metal *s* electrons are transferred to the oxygen ions, and the remaining *d* electrons are strongly correlated and determine the physical properties of these complex oxides including electrical transport, magnetism, optical response and thermal conductivity. These electron correlations constrain the number of electrons at a given lattice site, and induce a local entanglement of the charge, spin

and orbital degrees of freedom and give rise to a variety of macroscopic phenomena like Mott insulators, various charge, spin and orbital orderings, metal–insulator transitions, multiferroics and superconductivity. In recent years, there has been a burst of activities to manipulate these phenomena, as well as to create new ones, using oxide heterostructures. As described in detail by Hwang *et al*. [105] the fundamental basis for understanding the physical properties of TMOs is the concept of the symmetry of the order parameter. As Landau has already stated, the essence of phase transitions is the change in symmetry. Manipulating the symmetry at an nanoscale level opens the door for artificially designed phase transitions. The interplay among the electronic degrees of freedom produces various forms of symmetry-breaking patterns of space inversion, time-reversal and gauge symmetry (associated with the change of the phase of the wave function) and is expected to lead to novel emergent phenomena triggered through the collective behavior of electrons.

An especially intriguing case is the combination of ferromagnetic (FM) and superconducting (SC) oxide layers as heterostructures and superlattices. Phenomenologically, ferromagnetic and superconducting order has been regarded to be antagonistic by nature for a long time. Ferromagnetic order consists in the parallel alignment of spins whereas for the essential ingredient of superconductivity, the Cooper pairs, the coupling of electrons with antiparallel spin is mandatory. In this section some of the experiments are reviewed which contributed to the boom of research activities in complex oxide interface investigations. Amongst them are the early activities to grow and analyze SC/FM heterostructures and superlattices, the determination of the spin diffusion length in the superconductor and the growth of SC/FM bi- and trilayers for potential use in planar SFS junctions.

4.2. Ferromagnet-superconducting bilayers and superlattices

4.2.1. Early experiments

In conventional *s*-wave superconductors local magnetic moments break the spin singlet Cooper pairs and thus strongly suppress superconductivity. There is, however, a limited class of superconducting compounds where superconductivity occurs in the presence of magnetic ions occupying a specific lattice site. Some examples are the rare earth molybdenum selenides (RMo_6Se_8) and the rare earth rhodium borides (RRh_4B_4). All these materials have in common that the superconducting ordering temperature is substantially higher than the Curie temperature. A comprehensive review of the physics of the coexistence of ferromagnetism and superconductivity in these materials is given by Maple [109]. The discovery of ferromagnetism and superconductivity in a completely different class of materials, the cuprate based compound $RuSr_2GdCu_2O_8$ (Ru1212) [110] generated much interest mainly due to the fact that the Curie temperature is much higher (~ 160 K) than the superconducting T_c, (~ 50 K), i.e. superconductivity emerges in a magnetic environment. Since in copper oxides superconductivity appears upon doping of an antiferromagnetic parent compound a detailed analysis of the properties of $RuSr_2GdCu_2O_8$ can shed some light on the origin of superconductivity in the cuprates. Structurally, Ru1212 consists of a charge reservoir block containing magnetically ordered Ru^{5+} ions intercalated by CuO_2–Gd–CuO_2 layers which are believed to cause superconductivity. Due to the layered structure of Ru1212 a natural extension for the research on magnetic superconductors was to mimic its properties by combining oxide ferromagnmets (e.g. LaCaMnO) and oxide superconductors (YBCO) in heterostructures and superlattices. Stimulated by earlier studies of cuprate/manganite heterostructures [111] Habermeier *et al*. performed systematic studies by varying the individual layer thicknesses in superlattices and studied their transport and magnetic properties [112]. The films grown by PLD showed x-ray diffraction patterns of a superposition of features from YBCO and LCMO including superlattice peaks indicating the perfection of their crystallographic structure as shown in Fig. 20.

Figure 21(a) depicts the temperature dependence of resistance as well as the magnetization for an n/m YBCO/LCMO superlattice evidencing the existence of a strong interaction between the SC and FM order parameter, indicated by the reduction of both ordering temperatures. At the beginning of these research activities there has been much concern about sample quality and how they can affect the results. Reproducibility of the results — even quantitatively — by different groups and detailed microstructural analysis including analytical high resolution TEM could rule out these concerns [113]. Figure 21(b), e.g., displays a high resolution TEM micrograph of an YBCO/LCMO SL in the vicinity of the STO substrate showing the structural perfection of the YBCO and LCMO layers and the structurally perfect interface.

Additionally, it could be shown by dedicated analytical TEM investigations that the interfacial stacking patterns are different for the YBCO–LCMO interface (YBCO–BaO–CuO_2–(La,Ca)O–MnO–LCMO and the LCMO–YBCO one (LCMO–(La,Ca)O–MnO–BaO–CuO–BaO–CuO_2–YBCO) [114]. The consequences of the details of the microstructure on the macroscopic properties of the films are not explores yet, however, they might be of importance for the charge carrier transport across the interfaces The early work on these hybrid structures and superlattices composed of a high temperature superconductor (e.g. YBCO) and a half metallic ferromagnetic oxide (e.g. LCMO) has initiated further activities to explore the interference between these antagonistic order parameters. Research on these structures has revealed charge transfer across the interfaces as well as interfacial spin and orbital polarization with consequences for the macroscopic properties including charge transport and thermoelectricity.

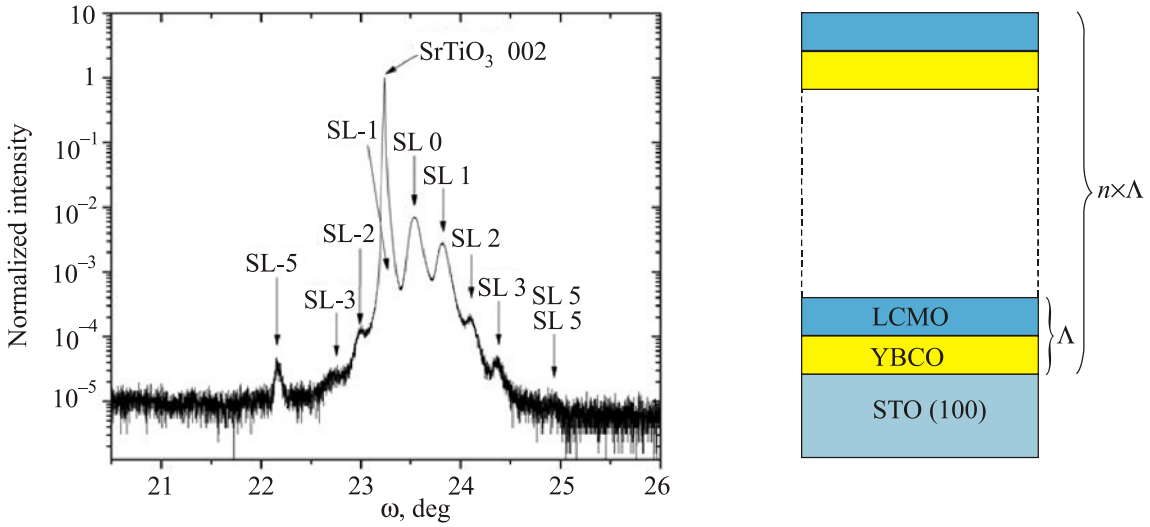

Fig. 20. (Color online) X-ray diffraction pattern of a YBCO/LCMO $(10/10)_{12}$ superlattice

4.2.2. Determination of the spin diffusion length

Measurements of the far infrared dielectric properties of these superlattices by spectroscopic ellipsometry provided clear evidence that due to the interaction of the ferromagnetic LCMO and the superconducting YBCO in the superlattices the free carrier response is strongly suppressed with an unexpected large length scale in the order of 10–20 nm. Control experiments replacing the FM LCMO layer by the paramagnetic $LaNiO_3$ metal do not show this suppression, so the suppression is due to the magnetic interaction [115]. Further evidence for the long range interaction came from an analysis of the T_c reduction in LCMO/YBCO bilayer samples [116]. In this experiment on top of a 20 nm LCM film deposited on STO or LSAO substrates YBCO films have been grown with thicknesses ranging from 20 to 100 nm and the temperature dependence of the magnetic response as well as their resistance

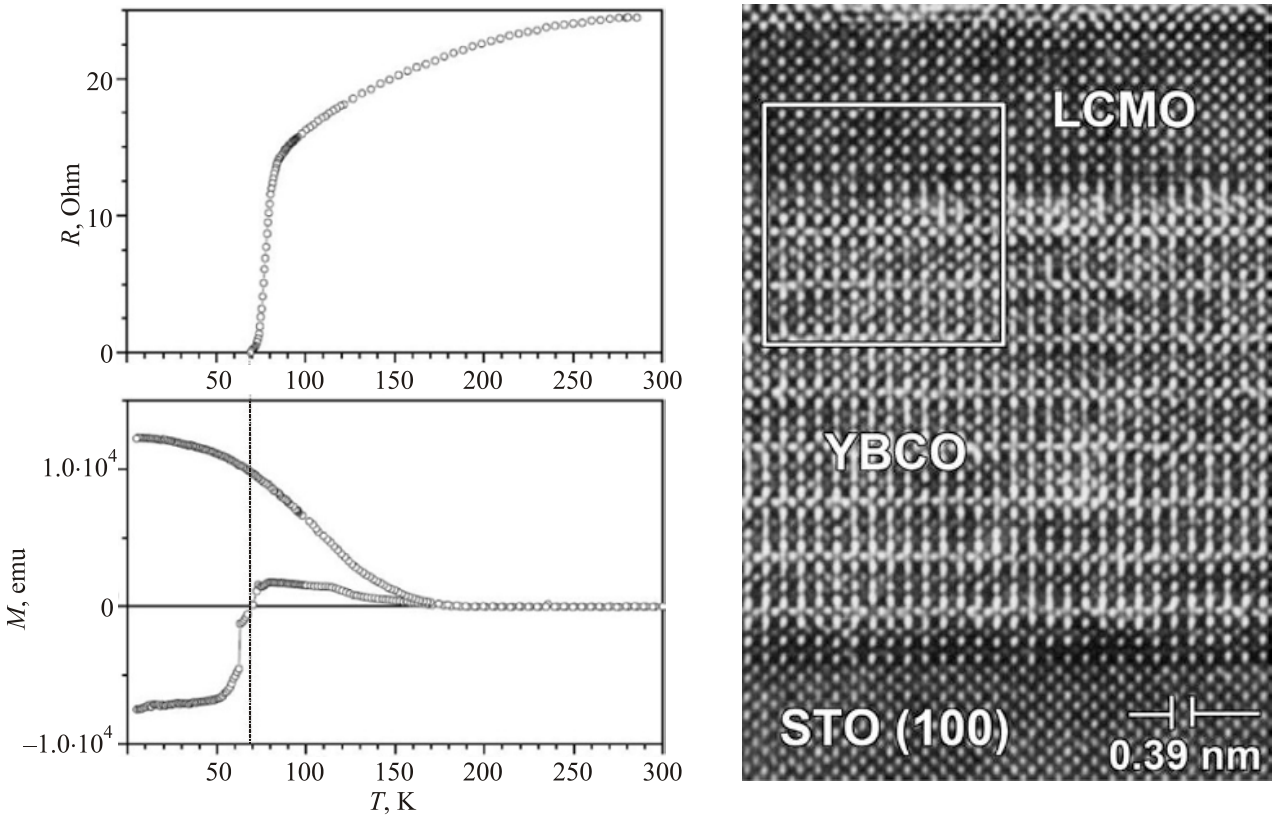

Fig. 21. Temperature dependence of resistance and the magnetic moment of a $(50nm/20nm)_5$ YBCO/LCMO superlattice (left) and a corresponding HRTEM (right).

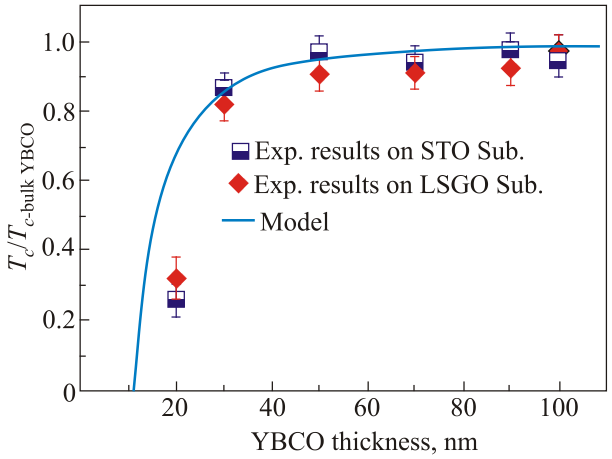

Fig. 22. (Color online) Normalized superconducting transition temperature of bilayers with varying thickness of the YBCO layer on STO_3 and $LSGO_4$ substrates obtained from the diamagnetic onset in the zero-field-cooling magnetization measurement (solid line) [116].

have been measured. Using the LCMO as an electrode the role of spinpolarized quasiparticle injection into YBCO and the corresponding reduction of T_c could be investigated. Using a classical model by Parker [117] the pair breaking effect of spinpolarized quasiparticle injection into YBCO was compared with the experimental results and the comparison revealed that the pair breaking effect due to the spinpolarized quasiparticle injection is found to be ~10 nm compatible with the results from Holden [115].

Figure 22 shows the excellent agreement of the experimental results for YBCO films of different thickness deposited on 20 nm LCMO in comparison with the theoretical model. These experiments clearly show that the interaction between the SC and the FM layer in the heterostructures and superlattices are not confined to a length scale of a few nm, only.

4.2.3. (*110*)*-oriented* YBCO/LCMO *heterostructures and trilayers*

As already stated, superlattices and heterostructures of transition metal oxides with strong electron correlations are gaining increasing interest as a platform to harness a variety of quantum many-body states (including metal-insulator transitions, ferromagnetism, superconductivity, multiferroicity, as well as charge, spin, and orbital ordering) for potential applications. Using structures composed of two or more TMOs, interference between these states across interfaces has the potential to generate new phenomena and functionalities. Due to growth related technological boundary conditions, most of the superlattices and heterostructures investigated so far were grown along the [001] axis of the YBCO crystal structure. Here, the direction perpendicular to the highly conducting CuO_2 planes is parallel to the YBCO–LCMO interface. The role of proximity coupling of superconducting and ferromagnetic order parameters has not yet been clarified in these structures, presumably as a consequence of the small superconducting coherence length $\xi_c \sim 0.3$ nm of YBCO in the [001] direction. Investigations of films with the much larger coherence length $\xi_{ab} \sim 1.6$ nm oriented perpendicular to the film plane can shed more light at the proximity coupling. Mustafa *et al.* [118] deposited heterostructures using pulsed laser deposition with deposition parameters optimized for the growth of (110)-oriented YBCO films. Due to the problems of the competing (110) and (103)/(10$\bar{3}$) orientations, Mustafa made pole figures choosing the YBCO (117) orientation with no overlap with any of the STO or LCMO reflections (Fig. 23(a)). The absence of such reflections in the pole figures clearly demonstrates that the films are exclusively (110) oriented, within the detection limit of x-ray diffractometry. To check the orientation of the LCMO layer with respect to the substrate and the YBCO layer, the (116) plane of LCMO was chosen for an additional set of pole figures (Fig. 23(b)). Here, 12 peaks are observed in the scan, eight of which refer to reflections from the STO (221) plane, and four of which arise from the (116) reflection (or equivalent reflections) of LCMO. No other peaks of LCMO were observed, indicating that the LCMO layer is grown epitaxially with its (110) plane parallel to the (110) plane of STO. The pole figure analysis of the heterostructures thus demonstrates that the (110) planes of the STO substrate, the YBCO layer, and the LCMO layer are parallel to each other. Figure 24 presents the temperature dependence of the resistivity measured perpendicular (ρ_{ab}) and parallel (ρ_c) to the YBCO *c*-axis using a standard four-probe arrangement (inset in Fig. 24). The large anisotropy ($\rho_c/\rho_{ab} \sim 25$ at room temperature, ~ 35 at 180 K) is consistent with the single-phase nature of the film inferred from the structural analysis and is caused by the resistivity anisotropy of YBCO. The temperature dependence of the resistivity of the film can be modeled as a network of parallel resistors and is hence dominated by the layer with the smallest resistivity. In the direction of the CuO_2 planes the value is dominated by the YBCO layer whereas in the perpendicular direction both resistivities (YBCO and LCMO, respectively) are of comparable magnitude and contribute nearly equally to the total value.

The contribution of the LCMO layer can be recognized in the resistivity peak around the Curie-temperature that is typical for ferromagnetic LCMO films. This contribution is presumably responsible for the lower resistivity anisotropy of the film compared to bulk YBCO, where $\rho_c/\rho_{ab} \sim 100$ at optimal doping. Both resistivity curves reveal a superconducting transition with an onset around 90 K, and zero resistivity (within the measurement error) around 75 K. The rounding of the superconducting transition may reflect intrinsic interfacial effects (such as the transfer of spinpolarized quasiparticles across the interface) and/or residual inhomogeneity of the oxygen content within the YBCO

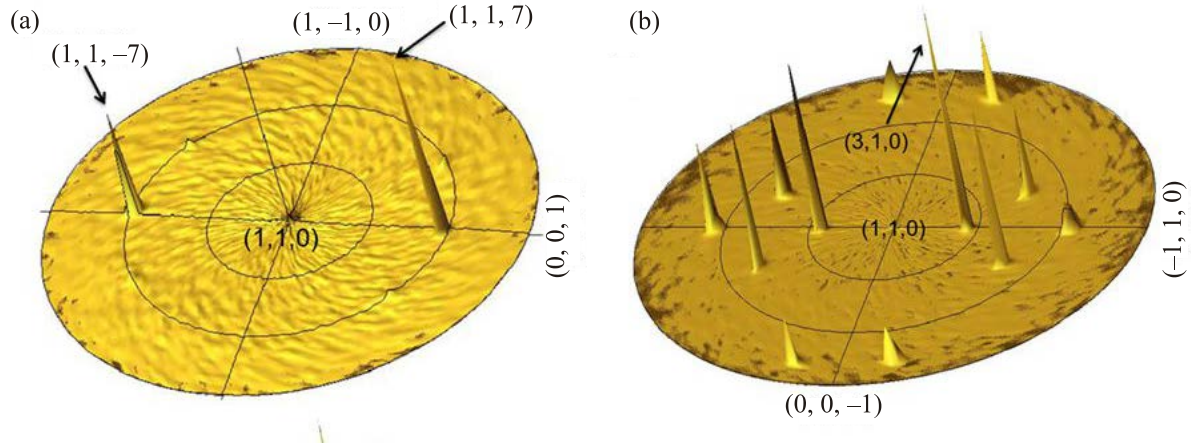

Fig. 23. (Color online) X-ray pole figures of an LCMO (50 nm)–YBCO (100 nm) heterostructure (a) around the (117) reflection of YBCO, and (b) around the (116) reflection of LCMO [118].

layer. The technological progress accomplished by Mustafa *et al.* [118] offers the opportunity to contribute to the investigation of the interrelation between crystallographic and electronic structures and thus to the interface properties. The comparison of the reduction of T_c in (001) and (110) — oriented bilayer (82 K for (001) and 60 K for (110)) indicates that the extension of the proximity effect between ferromagnetic and superconducting layers arises from the different coherence length. The different atomic stacking of the constituents and thus their electronic configuration of (001) and (110) oriented bilayers can be used as a control parameter to achieve deeper insight in the fundamental physics of these heterostructures.

The extension of this so far more technological work is the fabrication of hybrid oxide superconductor/ferromagnet/superconductor (SFS) structures with potential applications in superconducting electronics and quantum computing. The understanding of the mechanism of the electrical transport across the oxide ferromagnetic barrier is the property of interest. Soltan *et al.* [119] showed that an ultra-thin LCMO ferromagnetic layer with a thickness of few unit cells can be grown in between of two thick YBCO superconducting layers. In particular, the ferromagnetic transition temperature is found to be T_{Curie} = 260 K which is close to the bulk value This opens up the way to investigate the electronic transport across the thin ferromagnetic layer with possible perspectives: (i) to fabricate oxide SFS Josephson junctions and (ii) to understand in detail the proximity effects in oxide SFS-structures with strong correlation. Therefore the successful fabrication of oxide SFS-structures may help to understand the long-range proximity

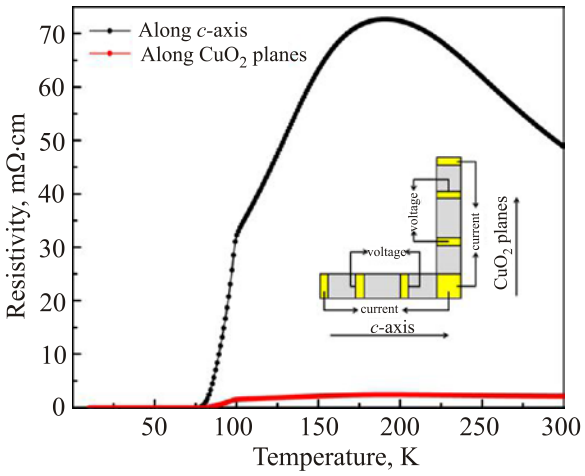

Fig. 24. (Color online) Temperature dependence of resistivity of an LCMO (50 nm)–YBCO (100 nm) heterostructure parallel and perpendicular to the YBCO *c*-axis. The inset shows the arrangement of Au contact pads evaporated on the film surface [118].

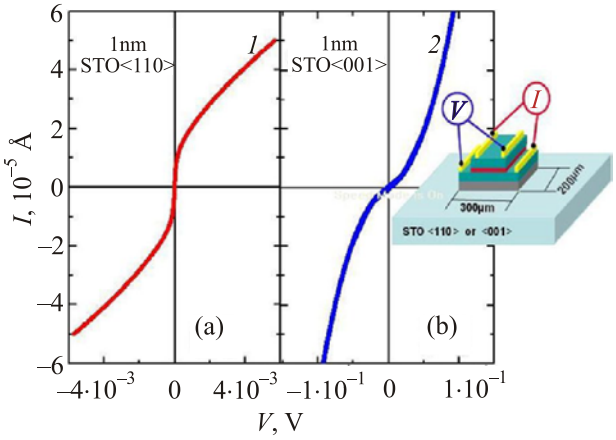

Fig. 25. (Color online) Current-voltage curves of current transport across the ferromagnetic barrier. Junctions with lateral dimensions of 300 μm × 200 μm were prepared by ion milling out of the heterostructures of YBCO–LCMO–YBCO (50 nm–1 nm–50 nm) grown on STO-110 (red, *1*) and 001 (blue, *2*). A sketch is shown in the inset of panel (b). (a) — the *I*–*V* curve of the 110-sample shows a vertical slope at $V = 0$ indicating a superconducting transport with critical current of $1 \cdot 10^{-5}$ Å. (b) — the *I*–*V* curve of the 001-sample shows nonlinear behavior for *I*–*V* curve without any supercurrent flowing at $V = 0$ [119].

effects between *d*-wave high-T_c superconductors and half-metal ferromagnetic LCMO layers. The main difficulty in accomplishing this type of junctions is a technological one and arises from the length scale required to obtain a supercurrent. Charge transfer, spin-polarized effects as well as structural effects at the interface can strongly suppress superconducting transport across the oxide ferromagnetic interface. The conjecture is that the thickness of the ferromagnetic LCMO barrier must be comparable to the superconducting coherence length.

Soltan *et al*. succeeded in fabricating ultra-thin ferromagnetic LCMO layers in between two epitaxially grown YBCO films with different crystallographic orientations, namely, (110) and (001). They could observe a clear and unexpected ferromagnetic response of 1 nm and 2 nm thick LCMO films with ordering temperatures above $T \approx 200$ K. In combination with YBCO films grown in (110)-orientation using sophisticated buffer layers, it is possible to realize a high-T_c SFS-junction with a ferromagnetic layer thinner than the coherence length ξ_{ab} of YBCO. The measurements give evidence of supercurrent transport across the ferromagnetic barrier (Fig. 25). Barrier roughness and temperature and field dependence of the transport current strongly suggest that the observed transport current is flowing at least partly across the ferromagnet.

4.3. Ferromagnet–superconductor interfaces

4.3.1. General remarks

Artificial superlattices (SL's) represent a well-established research topic in condensed matter physics and modern device technology. Semiconductor heterostructures and SL's have proven to form the basis for unexpected advances in science and device physics over the past decades. The development of solid state lasers and high electron mobility transistors (HEMT) may serve as prototypes for the advances in device physics. An example for achievements in basic science is the formation of a 2-dimensional electron gas in III–V-compound semiconductor heterostructures or in silicon metal-oxide-semiconductor field-effect transistors enabling the subsequent discovery of the quantum Hall effect by von Klitzing *et al*. [120]. Similarly, metallic SL's consisting of paramagnetic and ferromagnetic layers give rise to a giant magnetoresistance [121] and serve now as sensing elements in reading heads of hard disk drives. The attempt to replicate such SL's using transition metal oxides (TMO's) and explore their rich potential in "orbital physics" will pave the way for an even more exciting research area. The delicate interplay of spin-, charge-, orbital and lattice interactions of electrons arising from charge transfer across the interface and the sensitivity of the orbital ordering patterns of electrons in the 3*d* shells to external perturbations such as strain, electrical and magnetic fields, photon flux etc. can open a wide field of applications. Combining such TMO's into heterostructures (HS's) or SL's gives rise to expectations that at their interfaces novel correlation driven quantum states are appearing with functionalities qualitatively beyond those attainable in metals or semiconductors. Since the physical properties of TMOs are often dominated by the state variables of the *d*-electrons, a natural starting point for the study of heterostructures, combining different TMO's is the investigation of their configurations at the interfaces is. There are intense efforts addressing this general issue including changes of the *d*-electron configuration by electrostatic boundary conditions that lead to conducting layers at the insulator interface of $SrTiO_3$ and $LaAlO_3$. In a review paper Hwang *et al*. [105] addressed these issues in more general terms and discussed the science of oxide interfaces from the viewpoint of emergent phenomena due to strong electron correlations. Combining advances in experimental techniques and new concepts supported by first-principles electronic structure calculations, the oxide HS's and SL's will be an ideal arena for physics, chemistry and technology in the years to come.

Whereas in the previous section the focus was more on technological achievements and interlayer interactions, in this section the more fundamental physics driven research activities such as the interplay of charge transfer across and orbital reconstruction at the interface are briefly reviewed.

As shown in Sec. 4.2. the technological requirements to prepare YBCO/LCMO heterointerfaces in a reproducible way are accomplished to a high degree of perfection. Tailoring the film orientation can be used to exploit the anisotropy of the correlation lengths of the compounds involved — an area exploited so far from the technological point of view only. In order to be able to focus on the physics of interfaces and their intentional manipulation in addition to precision in the sample preparation, the availability of the appropriate analytical tools for their characterization is mandatory. Structural analysis by conventional area averaging x-ray diffraction techniques and local high resolution transmission electron microscopy have to be supplemented by more sophisticated local element specific diagnostic tools to shed some light on the microscopic mechanisms taking place at the interfaces.

Analytical high resolution TEM with element specific resolution down to the atomic level will help to structurally characterize films and interfaces. Complementary Electron Energy Loss Spectroscopy (EELS) in a TEM is a powerful tool to reveal structural and chemical element specific information of solids with atomic resolution. The obvious disadvantage of all TEM techniques is the rather sophisticated destructive preparation of the films to be investigated into electron transparent samples with caveats to generate artifacts due to the thinning process. In contrast to TEM, the x-ray techniques are nondestructive, eventually element specific probes with the ability to study the behavior of electrons at the interfaces — typically buried several nanometers below the surface. In the book by Willmott these mainly synchrotron based techniques are described [122].

Resonant x-ray absorption spectroscopy exploits the properties of x-ray beams from a synchrotron. Their absorption length is typically more in the μm range rather than in the nm range thus penetrating deeply into the samples, enabling the analysis of the properties of buried layers. The photon energy directed to the sample can be tuned and their polarization parallel and perpendicular to the interface can be used to extract information about the shape of the valence-electron clouds (orbitals) around these atoms. The total electron yield and the fluorescence yield are the quantities to be measured. Resonant elastic x-ray scattering (REXS) provides a sensitive probe for spatial modulations of spins, charges, and orbitals. This unique sensitivity is achieved by merging diffraction and x-ray absorption spectroscopy (XAS) into a single experiment, where the scattering provides information about spatial modulations and the XAS provides sensitivity to the electronic structure. More precisely, resonant x-ray scattering close to an absorption edge involves virtual transitions from core levels into unoccupied states close to the Fermi level and these virtual transitions depend strongly on the spin, charge and orbital configuration of the resonant scattering centers. Furthermore, the resonance process strongly enhances the scattering cross-section and allows the opportunity to study selected atomic species in a crystal. Resonant inelastic x-ray scattering (RIXS) experiments, in which one scatters x-ray photons inelastically, probes the changes in energy, momentum, and polarization of the scattered photon from intrinsic excitations of the material under study. RIXS is able to probe many elementary excitations such as plasmons, charge-transfer excitations, crystal-field and orbital excitations, magnons, and phonons. Besides, similar to REXS, the resonance in RIXS greatly enhances the cross-section and adds selectivity to atomic species. In this aspect, RIXS offers a wide landscape in the study of strongly correlated electron systems. Combining conventional techniques such as macroscopic measurements of the temperature dependence of resistivity and magnetic response of the samples with more advanced resonant x-ray techniques is a mandatory prerequisite to get a deeper insight into the processes taking place at the interfaces.

4.3.2. YBCO-LCMO *interfaces*

The observations described in Sec. 4.2. gave a strong hint that the macroscopic properties of the YBCO–LCMO heterostructures and superlattices are determined to a great deal by the interfaces at an atomic scale. To shed some light on the electronic mechanisms responsible for these observations samples with chemically pure, atomically sharp interfaces are required for both to accurately study the electronic interactions to the interface. The question to be addressed is how magnetism is affecting the electronic properties of the interfaces. Chakhalian *et al*. [123] and subsequently other research groups [124,125] applied the experimental diagnostic machinery described above to reveal the details of the electronic structure at the YBCO/LCMO interfaces. Experiments using spin-polarized neutron reflectometry [126] showed a strong magnetic contribution coming from the interface. Originally, Chekhovian *et al*. used symmetric YBCO–LCMO (10×10 nm) superlattices for the investigations and found a symmetry forbidden neutron-diffraction peak popping up at temperatures corresponding to the Curie temperature of the film. Resonant x-ray magnetic dichroism experiments revealed that there is an antiferromagnetic coupling of the Cu spins and Mn spins at the interface that is not compatible with the Goodenough–Kanamori–Anderson rules for the exchange interactions in oxides. Figure 26 shows the results of the XMCD measurements. Whereas in YBCO the conducting electrons are located in the $d_{x_2-y_2}$ orbitals, the ground state of LCMO is regarded to be an orbitally disordered state with fluctuating $d_{x_2-y_2}$ and $d_{3z_2-r_2}$ orbitals it is expected that the superexchange interaction for the Mn–O–Cu molecule would result in a ferromagnetic coupling in contrast to the experimental result. Further evidence for this scenario of an oribital reconstruction comes from the comparison of resonant linear dichroism experiments in the total electron yield and fluorescence modes in comparison with bulk YBCO data. The results represented in Fig. 27 clearly show that the electronic structure of the CuO_2 layer is modified by covalent bonds across the interface. These results suggest that the orbital rearrangement and strong hybridization are at least partially responsible for the unusual magnetic behavior previous-

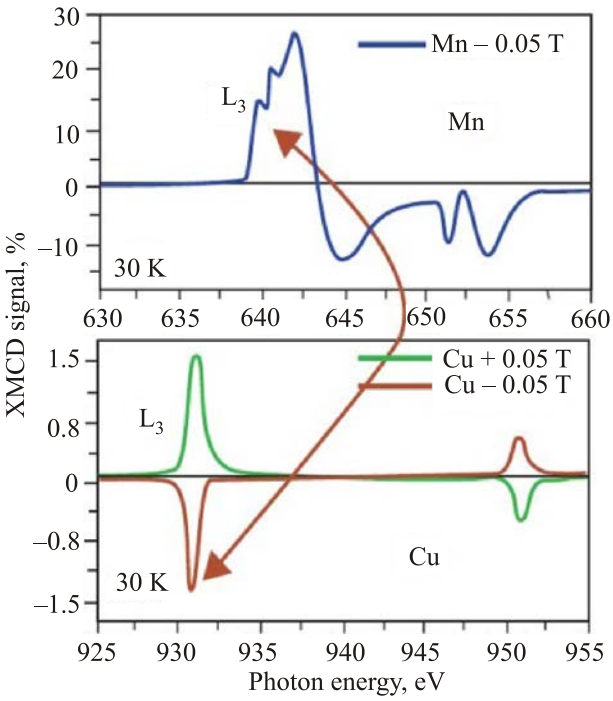

Fig. 26. (Color online) XMCD signals obtained from the core-level absorption spectra for Cu and Mn showing the antiferromagnetic coupling of the Mn and Cu spins [123].

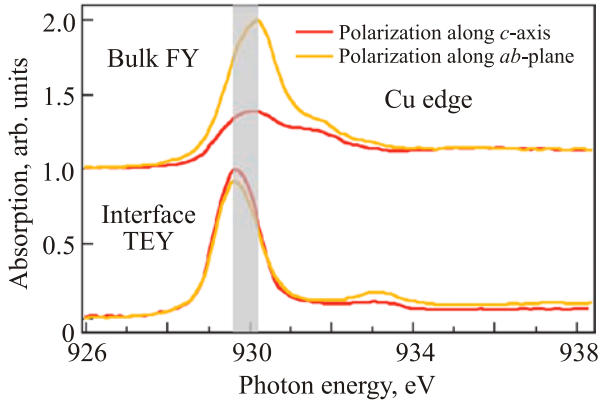

Fig. 27. (Color online) Normalized x-ray absorption spectra at the Cu L3 absorption edge, taken in bulk sensitive (FY, top panel) and interface sensitive (TEY, bottom panel) detection modes with varying photon polarization as indicated in the legend [127].

ly observed at cuprate-manganate interfaces and contribute to the suppression of superconductivity close to the interface. It is obvious that this mechanism of orbital reconstruction does not exclusively apply to the YBCO/LCMO interface but can be conjectured to apply for other transition metal oxides with nearly degenerate *d*-orbitals such as titanates, vanadates, ruthenates and ferrites.

5. Summary and future perspectives

Research in high temperature superconductivity has generated a tremendous amount of results during the past three decades. From the materials science point of view bulk processing and thin film deposition technology are the main fields of interest, both with an impact enabling applications. However, even after three decades there are plenty of fundamental questions to be solved before the focus can be shifted towards applications. The knowledge associated with the flux-line behavior in copper oxide superconductors and especially flux-line pinning is not yet at a stage where the mechanisms for pinning and thus the current-carrying capacity of superconducting wires are fully understood.

Thin film technology experienced a tremendous boost during this period. Pulsed Laser Deposition developed to be the working horse for complex oxide thin film and heterostructure fabrication. The availability of UV-excimer lasers with steadily increasing beam homogeneity and constant pulse-to-pulse energy was one technical prerequisite for this development. Furthermore, the exploration of the details of the PLD process has been extremely helpful to improve the film quality in the past decades (e.g. for YBCO). One of the benefits of PLD is the relative ease to fabricate not only single layer films of complex oxides but also heterostructures and superlattices with perovskite-type complex oxide materials having different functionalities. The precision of PLD thin film growth could be enhanced using RHEED control and thickness accuracy down to one unit cell can be achieved. Oxide- MBE has been demonstrated to be the method of choice as an excellent research tool to grow single layer films with superior perfection and to achieve sub-unit cell layer-by-layer deposition thus overcoming the limitations of PLD. The future in thin film technology is seen in a further development of PLD to understand the plume formation better and find ways to manipulate and analyze the plume formation process.

Albeit the diagnostic tools to analyze the properties of complex oxide thin films have improved in the past decade to an unprecedented degree, especially in the field of advanced Transmission Electron Microscopy and Synchrotron-based resonant x-ray techniques, the ultimate goal of element specific analysis with atomic resolution in conjunction with sensitivity to the electronic structure is not yet achieved.

The development of the experimental "machinery" ranging from dedicated sample preparation and analysis has opened — at least in the thin film case — the wing of a door into a new territory, the oxide interface research. Oxide interfaces are on the one hand an opportunity for novel types of electronics [106] and on the other hand the technological advances in the atomic scale synthesis of films enable the access to so far barely explored novel states at the interfaces. A rich playground for materials based curiosity inspired physics is emerging with bright perspectives for science and potential applications.

Acknowledgements:

The author is highly indebted to the current and previous members of the Technology Group of the Max-Planck-Institute for Solid State Research, Stuttgart, for their enthusiasm in the thin film work for complex oxides. He benefitted much from in-depth discussions with M. Cardona, B. Keimer and O.K. Andersen and the members of their departments. The financial support of the Max-Planck-Society, the German Science Foundation (DFG) as well as the European Union within the frame of several EU-NMP projects is greatly appreciated.

1. D. van Delft and P. Kess, *Phys. Today* **63**, 38 (2010).
2. S. Blundell, *Superconductivity: A Very Short Introduction*, Oxford University Press (2009).
3. B. Matthias, *Phys. Rev.* **87**, 380 (1953).
4. T. Berlincourt and R.R. Hake, *Phys. Rev. Lett.* **9**, 293 (1962).
5. G.F. Hardy and J.K. Hulm, *Phys. Rev.* **89**, 884 (1952).
6. J.R. Gavaler, *Appl. Phys. Lett.* **23**, 480 (1973).
7. H.-U. Habermeier, *Phys. Status Solidi A* **64**, 157 (1981).
8. H. Fröhlich, *Phys. Rev.* **79**, 845 (1950).
9. J. Bardeen, L.N. Cooper and J. R. Schrieffer, *Phys. Rev.* **108**, 1175 (1957).
10. A.A. Abrikosov, *Sov. Phys.-JETP* **5**, 1174 (1957).
11. G.M. Eliashberg, *Sov. Phys. JETP* **11**, 696 (1960).
12. J.G. Bednorz and K.A. Müller, *Z. Phys. B* **64**, 189 (1986).

13. V.J. Emery, *Phys. Rev. Lett*. **58**, 2794 (1987).
14. M.K. Wu, J.R. Ashburn, C.J. Torng, P.H. Hor, R.L. Meng, L. Gao, Z.J. Huang, Y.Q.Wang, and P. Chu, *Phys. Rev. Lett.* **58**, 908 (1987).
15. L. Gao, Y.Y. Xue, F. Chen, Q. Xiong, R. Meng, D. Ramirez, C.W. Chu, J.H. Egger, and H.K. Mao, *Phys. Rev. B* **50**, 4264 (1994).
16. e.g. *IEEE Trans. Appl. Supercond.* **25**, No. 3 (2015).
17. EUCAS e.g. *J. Phys. Conf. Ser*., IOP Publishing (2010).
18. B. Keimer, S.A. Kivelson, M.R. Norman, S. Uchida, and J. Zaanen, *Nature* **518**, 179 (2015).
19. F. Beech, S. Miraglia, A. Santoro, and R.S. Roth, *Phys. Rev. B* **35**, 8778 (1987).
20. J.D. Jorgensen, B.W. Veal , W.K. Kwok, G.W. Crabtree, A. Umezawa, L.J. Nowicki, and A.P. Paulikas, *Phys. Rev. B* **36**, 5731 (1987).
21. R.J. Cava, B. Batlogg, R.B. van Dover, D.M. Murphy, S. Sunshine, T. Siegrist, J.P. Remeika, E.A. Rietman, S. Zahurak, and G.P. Espinosa, *Phys. Rev. Lett*. **58**, 1676 (1987).
22. Patrick A. Lee, Naoto Nagaosa and Xiao-Gang Wen, *Rev. Mod. Phys*. **78**, 17 (2006).
23. P. Phillips, *Philos. Trans. R. Soc. A* **369**, 1574 (2011).
24. T.K. Worthington, W.J. Gallagher, and T.R. Dinger, *Phys. Rev. Lett*. **59**, 1160 (1987).
25. D. Dimos, P. Chaudhari, and J. Mannhart, *Phys. Rev. B* **41**, 4038 (1990).
26. M. Tinkham, *Introduct. Supercond.*, Dover Publications (1996).
27. K.K. Likharev and V.K. Semenov, *IEEE Trans. Appl. Supercond*. **1**, 3 (1991).
28. R. Wördenweber, *Supercond. Science and Technol*. **12**, R 86 (1999).
29. H. M. Christen and G. Eres, *J. Phys.: Condens. Matter* **20**, 264005 (2008).
30. H.-U. Habermeier and M. Hitchman (Edts.), *J. Alloys Comp.* **252**, 1–380 (2007).
31. H.-U. Habermeier, *Mater. Today* **10**, 34 (2007).
32. G. Koster, M. Huijben, and G. Rijnders, *Epitaxial Growth of Complex Metal Oxides*, Woodhead Publishing Series in Electronical and Optical Materials (2015).
33. R. Bormann and J. Nölting, *Appl. Phys. Lett.* **54**, 2148 (1989).
34. T.A. Vanderah, *Chemistry of Superconducting Oxides Noyes Publications*, N. Y. (1991).
35. I.D. Raistrik in: *Interfaces in High T_c Superconducting Systems*, S.L. Shinde and A. Rudman (eds.), Springer Verlag Berlin (1994)
36. R.E. Somekh in: *Concise Encyclopedia of Magnetic and Superconducting Materials*, J. Evetts (ed.), Pergamon Press, Oxford (1992), p. 431.
37. X.-Y. Zheng, D.H. Lowndes, S. Zhu, J. D. Budai, and R.J. Warmack, *Phys. Rev. B* **45**, 7584 (1992).
38. H. Zhang, *private communication*.
39. T. Terashima, Y. Bando, K. Iijima, K. Yamamoto, K. Hirata, K. Hayashi, K. Kamigaki, and H. Terauchi, *Phys. Rev. Lett*. **65**, 2684 (1990).
40. M. Varela, *Phys. Rev. Lett*. **86**, 5156 (2001).
41. E.K. Hollmann, O.G. Vendik, A.G. Zaitsev, and B.T. Melekh, *Supercond. Science Techn*. **76**, 609 (1994).
42. H.-U. Habermeier, *J. Electroceram*. **13**, 23 (2004).
43. M. Kawasaki, *Science* **266**, 1540 (1994).
44. G. Koster, *Appl. Phys. Lett*. **73**, 2920 (1998).
45. T. Haage, H.-U. Habermeier, and J. Zegenhagen, *Surf. Science* **370**, L158 (1997).
46. T. Haage, J. Zegenhagen, J.Q. Li, H.-U. Habermeier, M. Cardona, Ch. Jooss, R. Warthmann, A. Forkl, and H. Kronmüller, *Phys. Rev. B* **56**, 8404 (1997).
47. Z.-H. Wang, *Appl. Phys. Lett*. **82**, 3731 (2003).
48. P. Pahlke, S. Trommler, B. Holzapfel, L. Schultz, and R.H. Kühne, *J. Appl. Phys*. **113**, 123907 (2013).
49. J.P. Locquet, J. Perret, J. Fompeyerine, E. Machler, J.W. Seo, and G. Van Tendeloo, *Nature* **394**,453 (1998).
50. F.S. Razavi, G. Gross, H.-U. Habermeier, O. Lebedev, S. Amelinckx, G. Van Tendeloo, and A. Vigliante, *Appl. Phys. Lett*. **76**, 155 (2000).
51. J. H. Haeni, P. Irvin, W. Chang, R. Uecker, P. Reiche, Y.L. Li, S. Choudhury, W. Tian, M.E. Hawley, B. Craigo, A.K. Tagantsev, X.Q. Pan, S.K. Streiffer, L.Q. Chen, S.W. Kirchoefer, J. Levy, and D.G. Schlom, *Nature* **430**, 758 (2004).
52. C. Thiele, K. Doerr, O. Bilani, J. Rodel, and L. Schultz, *Phys. Rev. B* **75**, 054408 (2007).
53. R.K. Zheng, H.-U. Habermeier, H.L.W. Chan, C.L. Choy, and H.S. Luo, *Phys. Rev. B* **81**, 104427 (2010).
54. R.K. Zheng, Y. Wang, H.-U. Habermeier, H.L. W. Chan, X.M. Li, and H.S. Luo. *J. Alloys Comp*. **124**, 3807 (2012).
55. C.C. Tsuei, *Science* **263**, 1259 (1994).
56. B. Utz, *IEEE Trans. Appl. Supercond.* **7**, 1272 (1997).
57. A.J. Cho, *J. Vac. Sci. Technol*. **16**, 275 (1979).
58. K. Ploog, in: *Crystals; Growth Properties and Applications*, H.C. Freyhardt (ed.), Springer, Berlin (1980), Vol 3.
59. I. Bozovic, *Physica C* **235**, 178 (1994).
60. D.G. Schlom, J.H. Haeni, J. Lettieri, C. D. Theis, W. Tian, J.C. Jiang, and X.Q. Pan, *Mater Science Engin. B* **87**, 282 (1991).
61. S. Rossnagel, *J. Vac. Sci. Technol. A* **21**, 574 (2003).
62. P.R. Willmot, *Progr. Surface Science* **76**, 163 (2004).
63. U. Poppe, J. Schubert, R.R. Arons, W. Evers, C. Freiburg, W. Reichert, K. Schmidt, W. Sybertz, and K. Urban, *Solid State Commun*. **66**, 661 (1988).
64. J. Greek, G. Linker, and O. Mayer, *Mater. Sci. Rep*. **4**, 193 (1989).
65. C.B. Eom, J.Z. Sun, B.M. Lairson, S.K. Streiffer, A.F. Marshall, K. Yamamoto, S.M. Anlage,. J.C. Bravrnan, and T.H. Geballe, *Physica C* **171**, 354 (1990).
66. S.H. Liou, M. Hong, J. Kwo, B.A. Davidson, H.S. Chen, S. Nakahara, T. Boone, and R.J. Felder, *Appl. Phys. Lett*. **52**, 1735 (1988).
67. D. Dijkamp, *Appl. Phys. Lett*. **51**, 619 (1987).

68. D. Bäuerle, *Laser Processing and Chemistry*, Springer, Berlin, Heidelberg, New York (1996).
69. T.J. Jackson and S.B. Palmer , *J. Phys. D* **27**, 1581 (1994).
70. S, Otsubo, T. Minamikawa, Y. Yonezawa, A. Moritomo, and T. Shimizu, *Jpn. J. Appl. Phys.***29**, L73 (1990).
71. P.E. Dyer, R.D. Greenough, A. Issa, and P.H. Key, *Appl. Phys. Lett*. **53**, 534 (1988).
72. C Aruta, S. Amoruso, R. Bruzzese, X. Wang, D. Maccariello, F. Miletto Granozio, and U. Scotti di Uccio, *Appl. Phys. Lett*. **97**, 252105 (2010).
73. *Handbook of Superconducting Materials*, D. Cardwell and D. Ginley (eds), Institute of Physics Publishing, Bristol and Philadelphia (2003), p. 1569.
74. N. Newman and G. Lyons, *J. Supercond*. **6**, 119 (1993).
75. D. Koelle, R. Kleiner, F. Ludwig, E. Dantsker, and J. Clarke, *Rev. Mod. Phys*. **71**, 631 (1999).
76. T. Terashima, T. Murakami, M. Suzuki, and K. Moriwaki, *Appl. Phys. Lett*. **53**, 2232 (1988).
77. G. Linker, X.X. Xi, O. Meyer, Q. Li, and J. Geerk, *Solid State Commun*. **69**, 249 (1989).
78. C. Thomsen and M. Cardona, in: *Physical Properties of High Temperature Superconductors*, D.M. Ginsberg (ed.), World Scientific, Singapore (1989), p. 409.
79. H.-U. Habermeier, A.A.C.S. Lourenco, B. Friedl, J. Kircher, and J. Köhler, *Solid State Commun*. **77**, 683 (1991).
80. F.T. Dias, P. Pureur, P. Rodrigues, Jr., and X. Obradors, *Phys. Rev. B* **70**, 224519 (2004).
81. G. Blatter, M.V. Feigel'man, V.B. Geshenbein, A.I. Larkin, and V.M. Vinokur, *Rev. Mod. Phys*. **66**, 1125 (1994).
82. H. Theuss and H. Kronmüller, *Physica C* **177**, 253 (1991).
83. M. Oussena, P.A.J. de Groot, S.J. Porter, R. Gagnon, and L. Taillefer, *Phys. Rev. B* **51**, 1389 (1995).
84. L. Civale, A.D. Marwick, T.K. Worthington, M.A. Kirk, J.R. Thompson, L. Krusin-Elbaum, J.R. Clem, and F. Holtzberg, *Phys. Rev. Lett*. **67**, 648 (1991).
85. Th. Schuster, H. Kuhn, M.V. Indenbom, G. Kreiselmeyer, M. Leghissa, and S. Klaumünzer, *Phys. Rev. B* 53, 2257 (1996).
86. S. Senoussi, K. Frikach, and C. Colliex, *Physica C* **235–240**, 2767 (1994).
87. J. Mannhart, D. Anselmetti, J.G. Bednorz, A. Catana, Ch. Gerber, K.A. Müller, and D.G. Schlom, *Z. Phys. B* **86**, 177 (1992).
88. D.S. Misra, B.D. Padalia, S.P. Pai, R. Pinto, and S.B. Palmer, *Thin Solid Films* **245**, 186 (1994).
89. O. Eibl and B. Roas, *J. Mater. Res*. **5**, 2620 (1990).
90. H. Kronmuüller, Ch. Jooss, A. Forkl, R. Warthmann, H.-U. Habermeier, and B. Leibold, *Physica C* **266**, 235 (1996).
91. T. Haage, J. Zegenhagen, J.Q. Li, H.-U. Habermeier, M. Cardona, Ch. Jooss, R. Warthmann, A. Forkl, and H. Kronmüller, *Phys.Rev. B* **56**, 8404 (1997).
92. E.V. Thuneberg, *Cryogenics* **29**, 236 (1989).
93. R. Griessen, Wen Hai-hu, A.J.J. van Dalen, B. Dam, J. Rector, H.G. Schnack, S. Libbrecht, E. Osquiguil, and Y. Bruynseraede, *Phys. Rev. Lett*. **72**, 1910 (1994).
94. C.C. Tsuei, J.R. Kirtley, C.C. Chi, Lock See Yu-Jahnes, A. Gupta, T. Shaw, J.Z. Sun, and M.B. Ketchen, *Phys. Rev. Lett.* **73**, 593 (1994).
95. P.W. Anderson, *J. Phys. Chem. Solids* **11**, 26 (1959).
96. Ch. Jooss, R. Warthmann, H. Kronmüller, T. Haage, H.-U. Habermeier, and J. Zegenhagen, *Phys. Rev. Lett*. **82**, 632 (1999).
97. C.M. Varma, P.B. Littlewood, S. Schmitt-Rink, E. Abrahams, and A.E. Ruckenstein, *Phys. Rev. Lett*. **63** 1996 (1989).
98. A. Dubroka, M. Rössle, K.W. Kim, V.K. Malik, D. Munzar, D.N. Basov, A.A. Schafgans, S.J. Moon, C.T. Lin, D. Haug, V. Hinkov, B. Keimer, Th. Wolf, J.G. Storey, J.L. Tallon, and C. Bernhard, *Phys. Rev. Lett*. **106**, 047006 (2011).
99. A.L. Solovjov, H.-U. Habermeier, and T. Haage, *Fiz. Nizk. Temp*. **28**, 24 (2002) [*Low Temp. Phys*. **28**, 17 (2002)].
100. P.W. Anderson, *Phys. Rev. Lett*. **67**, 2092 (1991).
101. L.G. Aslamazov and A.I. Larkin, *Phys. Lett. A* **26**, 238 (1968).
102. K. Maki, *Prog. Theor. Phys.* **39**, 897 (1968); R.S. Tompson, *Phys. Rev. B* **1**, 327 (1970).
103. W.E. Lawrence and S. Doniach, in: *Proceedings of the Twelfth International Conference on Low Temperature Physics*; Kyoto (1971), p. 361.
104. A.L. Solovjov and V.M. Dmitriev, *Fiz. Nizk. Temp*. **35**, 227 (2009) [*Low Temp. Phys*. **35**, 169 (2009).]
105. H.Y. Hwang, Y. Iwasa, M. Kawasaki,, B. Keimer, N. Nagaosa, and Y. Tokura, *Nature Mat.* **11**, 103 (2012).
106. J. Mannhart and D.G. Schlom, *Science* **327**, 1607 (2010).
107. A. Ohtomo and H.Y. Hwang, *Nature* **427**, 423 (2004).
108. J. Chakhalian, J.W. Freeland, H.-U. Habermeier, G. Cristiani, G.G. Khaliullin, M. van Veenendaal, and B. Keimer, *Science* **318**, 1114 (2007).
109. M.B. Maple, *Physics C* **341–348**, 47 (2000).
110. C. Bernhard, J.L. Tallon, Ch. Niedermayer, Th. Blasius, A. Golnik, E. Brücher, R.K. Kremer, D.R. Noakes, C.E. Stronach, J. Ansaldo, *Phys. Rev. B* **59**, 14099 (1999).
111. G. Jakob, V.V. Moschalkov, Y. Bruynseraede, *Appl. Phys. Lett*. **66**, 2564 (1995).
112. H.-U. Habermeier, G. Cristiani , R.K. Kremer, O. Lebedev, and G. van Tendeloo, *Physica C* **364/365**, 298 (2001).
113. Z. Sefrioui, M. Varela, V. Peña, D. Arias, C. León, J. Santamaria, J.E. Villegas, J.L. Martinez, W. Saldarriaga, and P. Prieto, *Appl. Phys. Lett*. **81**, 4568 (2002).
114. Z.L. Zhang, U. Kaiser, S. Soltan, H.-U. Habermeier, and B. Keimer, *Appl. Phys. Lett*. **95**, 242505 (2009).
115. T. Holden, H.-U. Habermeier, G. Cristiani, A. Golnik, A. Boris, A. Pimenov, J. Humlicek, O.I. Lebedev, G. Van Tendeloo, B. Keimer, and C. Bernhard, *Phys. Rev. B* **69**, 064505 (2004).
116. S. Soltan, J. Albrecht, and H.-U. Habermeier, *Phys. Rev. B* **70**, 144517 (2004)
117. W.H. Parker, *Phys. Rev. B* **12**, 3667 (1975).
118. L. Mustafa, N. Driza, M. Le Tacon, H.-U. Habermeier, and B. Keimer, *Physica C* **505**, 70 (2014).

119. S. Soltan, J. Albrecht, E. Goering, G. Schütz, L. Mustafa, B. Keimer, and H.-U. Habermeier, *J. Appl. Phys*. **118**, 223902 (2015).
120. K. von Klitzing, G. Dorda, and M. Pepper, *Phys. Rev. Lett*. **45**, 494 (1980).
121. P. Grünberg, R. Schreiber, Y. Pang, M.B. Brodsky, and H. Sowers, *Phys. Rev. Lett.* **54**, 2442 (1986).
122. P. Willmott, *An Introduction to Synchrotron Radiation*, Wiley & Sons Ltd., New York (2011), Ch. 6.
123. J. Chakhalian, J.W. Freeland, G. Srajer, J. Strempfer, G. Khaliullin, J.C. Cezar, T. Charlton, R. Dalgliesh, C. Bernhard, G. Cristiani, H.-U. Habermeier, and B. Keimer, *Nat. Phys*. **2**, 244 (2006).
124. Z. Sefrioui, D. Arias, V. Pena, J.E. Villegas, M. Varela, P. Prieto, C. Leon, J.L. Martinez, and J. Santamaria, *Phys. Rev. B* **67**, 214511 (2003).
125. V. Pena, Z. Sefrioui, D. Arias, C. Leon, J. Santamaria, M. Varela, S.J. Pennycook, and J.L. Martinez, *Phys. Rev. B* **69**, 224502 (2004).
126. J. Stahn, J. Chakhalian, C. Niedermayer, J. Hoppler, T. Gutberlet, J. Voigt, F. Treubel, H.-U. Habermeier, G. Cristiani, B. Keimer, and C. Bernhard, *Phys. Rev. B* **71**, 40509 (2005).
127. J. Chakhalian, J.W. Freeland, H.-U. Habermeier, G. Cristiani, G. Khaliullin, M. van Veenendaal, and B. Keimer, *Science* **318**, 1114 (2007).